Chapter 14
Thermal Stability: Atomic Cohesive Energy

- *Critical temperature for phase transition depends on the atomic cohesive energy that is the product of bond number and bond energy.*
- *The skin of a solid generally melts prior to the bulk (supercooling) and some interfaces melt at temperatures higher than the bulk melting point (superheating).*
- *Group IIIa and IVa atomic clusters show superheating because of the bond nature evolution.*
- *A dual-shell model describes the T_C for ferromagnetic, ferroelectric, and superconductive phase transitions because of the involvement of both the long- and the short-range interactions.*
- *Activation energy for diffusion and epitaxial growth is proportional to the atomic cohesive energy; growing temperature controls the crystal size and associated properties.*

14.1 Cohesive Energy

14.1.1 Definition

The cohesive energy of a solid (E_{coh}) is an important quantity used to accounting for the binding strength of a crystal. The E_{coh} is equal to the energy dividing the entire crystal into the individually isolated atoms by breaking all bonds involved. The E_{coh} is given as: $E_{coh}(N) = NE_B = Nz_bE_b$, if no atomic CN imperfection is considered. The cohesive energy for an atom in the bulk, or atomic coherency, E_B, is the sum of the bond energy E_b over all its atomic CN, $E_B = z_bE_b$, for a specific atom in the bulk, $E_{Bz} = zE_z$ is the cohesive energy for an atom with z neighbors.

The heat required for releasing an atom from a solid is the right atomic cohesive energy. Phase transition by loosening the atom requires energy that is a fraction of the E_B. The atomic E_B varies with, not only the atomic CN, but also the CN

C. Q. Sun, *Relaxation of the Chemical Bond*, Springer Series in Chemical Physics 108, DOI: 10.1007/978-981-4585-21-7_14,

reduction induced bond strength gain. The under-coordinated surface atoms will be generally less thermally stable than those inside the core interior, unless the strength gain of the remaining bonds overcomes the effect of coordination reduction, $E_{Bz} > E_B$. For large bulk materials, effects of surface CN imperfection is negligible but, for small particles, surface effects become dominant because of the appreciably large fraction of such under-coordinated atoms at the surface.

The mean value of the E_{Bz} is responsible for the fall (undercooling) or rise (overheating) of the T_m of a surface and a nanosolid. The E_{Bz} is also responsible for other thermally activated behavior such as phase transition, catalytic reactivity, crystal structural stability, alloy formation (segregation and diffusion), and stability of electrically charged particles (Coulomb explosion), as well as the crystal growth and atomic diffusion, atomic gliding displacement that determine the ductility of nanosolids.

14.1.2 Known Mechanisms

14.1.2.1 Surface Area Difference

One approach to determine the E_{coh} of a nanosolid is to consider the difference between the surface area of the entire particle and the overall surface area of all the constituent atoms being isolated one from another [1]. For a spherical dot with R radius and N atoms of diameter d_0, the E_{coh} equals to the energy required to generate the area difference, ΔS, between the isolated N atoms and the nanodot without changing the volume:

$$\begin{cases} N4\pi(d_0/2)^3/3 = 4\pi(R)^3/3 & \text{(volume-conservation)} \\ \Delta S = \pi\left[Nd_0^2 - (2R)^2\right] & \text{(Surface-area-difference)} \end{cases}$$

Letting the surface energy per unit area at 0 K be γ_0, and then the overall $E_{coh}(N)$ is,

$$\begin{cases} E_{coh}(K) = \gamma_0 \Delta S & = \pi N d_0^2 \gamma_0 \left(1 - N^{-1/3}\right) \\ & = E_{coh}(\infty)(1 - \alpha/K) \end{cases}$$

$E_{coh}(\infty) = \pi N d_0^2 \gamma_0$ is the cohesive energy of the N atoms without the effect of atomic CN imperfection. The factor α varies with the shape and dimensionality of the solid. For a cube, the factor is 9/4 [1]; for a spherical dot, it is 1/2.

Considering situations of both the isolated and the embedded nanosolids with involvement of the interface and surface contributions [2]:

$$E_{B,s} = [E_B + 3\beta(E_B/2 + kE_m/2)]/4$$

yields the mean atomic cohesive energy,

$$\begin{aligned} E_{\mathrm{B}}(K) &= E_{\mathrm{B}} + \gamma_0\left(E_{\mathrm{B,S}} - E_{\mathrm{B}}\right) \\ &= E_{\mathrm{B}} + 3\gamma_0[k\beta E_{\mathrm{m}} - (2-\beta)E_{\mathrm{B}}]/8 \end{aligned}$$

where β is the ratio of the interface area to the entire surface area, k denotes the degree of cohesion between the nanocrystal and the matrix with atomic cohesive energy E_{B}. For a nanocrystal wholly embedded in the matrix, $\beta = 1$ and $k = 1$; for an isolated crystal, $\beta = 0$ and $k = 0$ [3].

14.1.2.2 Atomic CN Difference

By considering the effect of surface CN imperfection, Tomanek et al. [4] derived the E_{B} for an individual atom denoted i:

$$E_{\mathrm{B},i} = (z_i/z_{\mathrm{b}})^{1/2} E_{\mathrm{B}}(\infty) + E_R$$

E_{R} representing the repulsive interaction is negligible at equilibrium. The mean E_{B} in a nanosolid is obtainable by summing all bonds over all the N atoms:

$$\langle E_{\mathrm{B}}(N)\rangle = \sum_{\langle i,N\rangle} (z_i)^{1/2} E_i \Big/ N$$

A theory established based on the framework of the latent heat and the size-dependent cohesive energy agrees with experimental data results of W and Mo nanosolids [5].

14.1.3 BOLS Formulation

The BOLS notation considers variation of atomic E_{coh} from atoms in the skin only. Using the same spherical dot containing N atoms with N_i atoms in the ith surface shell, the average $\langle E_{\mathrm{coh}}(N)\rangle$, or $\langle E_{\mathrm{B}}(N)\rangle$ is,

$$\begin{aligned} \langle E_{\mathrm{coh}}(N)\rangle &= N z_{\mathrm{b}} E_{\mathrm{b}} + \sum_{i\le 3} N_i (z_i E_i - z_{\mathrm{b}} E_{\mathrm{b}}) \\ &= N E_{\mathrm{B}}(\infty) + \sum_{i\le 3} N_i z_{\mathrm{b}} E_{\mathrm{b}} (z_{i\mathrm{b}} E_{i\mathrm{b}} - 1) \\ &= E_{\mathrm{coh}}(\infty)\left[1 + \sum_{i\le 3} \gamma_i \left(z_{i\mathrm{b}} C_i^{-m} - 1\right)\right] \\ &= E_{\mathrm{coh}}(\infty)(1 + \Delta_{\mathrm{B}}) \\ \text{or, } \langle E_{\mathrm{B}}(N)\rangle &= E_{\mathrm{B}}(\infty)(1 + \Delta_{\mathrm{B}}) \end{aligned} \tag{14.1}$$

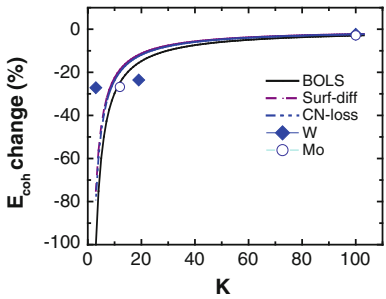

Fig. 14.1 Comparison of the modeling predictions with experimental results on the size-dependent E_B of Mo and W nanosolids [6]. Numerical agreement is nearly identical for the compared models albeit the different physical origins (Reprinted with permission from [7])

where $E_{coh}(\infty) = Nz_bE_b$ represents the ideal situation without CN imperfection. The $z_{ib} = z_i/z_b$ is the normalized *CN* and $E_{ib} = E_i/E_b \cong C_i^{-m}$ is the binding energy per coordinate of a surface atom normalized by the bulk value. For a free surface, $\Delta_B < 0$; for an intermixed interface, Δ_B may vary depending on the interfacial bond energy.

The following scaling relationships formulate the size dependence of E_B,

$$\frac{\Delta E_B(K)}{E_B(\infty)} = \begin{cases} \sum_{i\le 3}\gamma_i\left(z_{ib}c_i^{-m}-1\right) = \Delta_B & \text{(BOLS)} \\ \sum_{i\le 3}\gamma_i'\left[(z_{ib})^{1/2}-1\right] = \Delta_B' & \text{(CN-loss)} \\ -\alpha/K = \delta_B & \text{(Area-difference)} \end{cases} \tag{14.2}$$

where $\gamma_i \sim \tau C_i/\mathrm{K}$ and $\gamma'_i \sim \tau_i/K$ are the surface-to-volume ratio in the corresponding formulations. Figure 14.1 shows the match between these notations and measurements of the size-dependent $\langle E_B(K)\rangle$ of Mo and W nanosolids [6]. From a numerical viewpoint, one could hardly tell which model is preferred to others though physical indications of the compared models are different.

14.1.4 Atomic Vacancy Formation

As an element of structural defects, atomic vacancies, or point defects are very important in materials and have remarkable effect on the physical properties of a material such as electrical resistance, heat capacity, and mechanical strength. A vacancy formation is associated with local strain, densification, quantum entrapment, and polarization.

Atomic vacancy formation needs energy to break all the bonds of the specific atom to its surroundings, which is the same to the atomic E_B though structure deformation or relaxation is involved upon vacancy formation. However, the structural deformation or relaxation costs no additionally external energy. Vacancy volume should be greater than the atomic size because of the atomic CN imperfection induced contraction of bonds surrounding the vacancy. The measured E_B is subject to accuracy. For instance, the E_B of a Mo atom varies from 2.24 to 3.30 eV [8].

Theoretical efforts can predict the E_B of limited numbers of metals and alloys, but the theories are rather complicated [9].

14.1.4.1 Brook's Convention

Brooks [10] assumed the crystal is isotropic and considered the formation of a vacancy as an equivalent to creating new surface, equal to the area of one unit cell, being approximately the spherical surface of the atomic volume. He also assumed that the surface tension of the hole would shrink the vacancy size by distorting the rest of the crystal elastically. Then, the E_B for atomic vacancy formation inside a bulk solid equals the minimum of the sum of the increased surface energy and distortion energy,

$$E_B = \pi d_0^3 \gamma_0 G(\gamma_0 + G d_0)^{-1}$$

G is the shear modulus and γ_0 the surface energy per unit area surrounding the vacancy. Introducing the size effect to the d_0, G, and γ_0, the relative change in the mean E_B in a nanoparticle becomes,

$$\frac{E_p - E_B}{E_B} = \frac{d_p^3}{d_0^3}\left(\frac{G d_0 + \gamma_0}{G d_p + \gamma_0}\right) - 1$$

where E_p and d_p are the corresponding vacancy formation energy and mean atomic diameter in the nanosolid.

An extension of Brook's approach to nanostructures assumed that the G and the γ_0 of a nanosolid remain the bulk values [11]. The key factor influencing the E_p of a spherical dot of diameter D is the size-dependent atom size. Assuming that a small shrink of εD ($\varepsilon \ll 1$) results from the hole volume contraction, the surface energy variation $\Delta\gamma$, and the strain-dependent elastic energy f of the particle become,

$$\Delta\gamma = \pi D^2\left[(1-\varepsilon)^2 - 1\right]\gamma_0$$

$$f = \pi G D^3 \varepsilon^2 \tag{14.3}$$

At equilibrium, the total energy F, or the sum of $\Delta\gamma$ and f, is minimal, that is, $dF/d\varepsilon = 0$, and then, the strain of the particle becomes

$$\varepsilon = [1 + (G/\gamma_0)D]^{-1}$$

The average size d_p of an atom shrinks due to the presence of G and γ_0, $d_p = d_0(1-\varepsilon)$.

Table 14.1 Shear modulus, surface energy and the calculated α values for Pd and Au

	G (10^{10} N/m^2) [12]	γ_0 (J/m^2) [13]	α/nm	K_{Ec}/K_{dc}
Pd	4.36	2.10	0.104	0.1894/0.8770
Au	2.60	1.55	0.119	0.2066/1.035

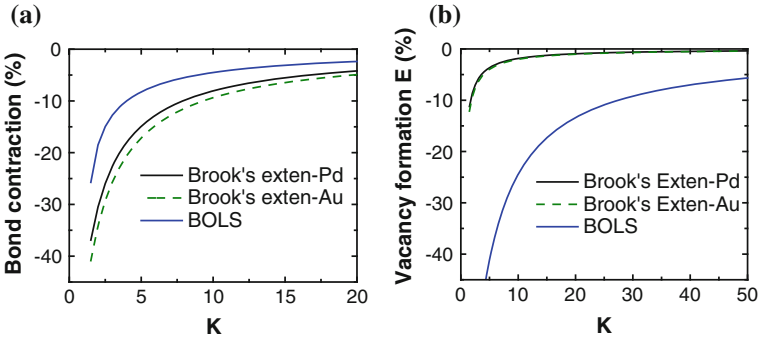

Fig. 14.2 Comparison of **a** the bond (particle size) contraction and **b** atomic vacation-formation energy derived from the BOLS premise and from Brook's approach for Pd and Au nanosolids (Reprinted with permission from [7])

14.1.4.2 BOLS Formulation

The following compares Brook's approximation and the BOLS correlation on the bond strain of a nanosolid:

$$\frac{\Delta d_p}{d_0} = \begin{cases} -[1 + (G/\gamma_0)D]^{-1} \cong -K_{dc}/(K + K_{dc}) & \text{(Brook)} \\ \sum_{i \le 3} \gamma_i (C_i - 1) = \Delta_d & \text{(BOLS)} \end{cases}$$

where $K_{dc} = \gamma_0/(2d_0G)$ is the critical value and K remains its usual meaning of dimensionless form of size. Further simplification of Eq. (14.3) leads to the atomic vacancy formation energy in a nanometric system as given in comparison with the BOLS derivative:

$$\frac{\Delta E_B(K)}{E_B(\infty)} = \begin{cases} -(1 + K/\alpha)^{-1} \cong -K_{Ec}/(K_{Ec} + K) \\ \sum_{i \le 3} \gamma_i \left(z_{ib} C_i^{-m} - 1\right) = \Delta_B \end{cases} \tag{14.4}$$

where $\alpha = (2gd_0 + 3)/[2d_0(g^2 d_0 + g)]$ ($\sim 10^{-1}$ level) and $g = G/\gamma_0 \sim 10$ nm^{-1}. $K_{Ec} = \alpha/(2d_0)$ is the critical value of K. For Pd and Au nanosolids, the critical K_{Ec} and E_{dc} values are calculated based on the given G and γ_0 bulk values, as listed in Table 14.1.

Figure 14.2 compares the predictions of the two models. At the lower end of the size limit ($K = 1.5$), the particle diameter contracts by 40 % associated with 12 % reduction in the E_B according to Brook's convention [11]. In comparison, the

BOLS correlation predicts a 25 % bond contraction and 70 % lower of the E_B for the smallest size. The approximation based on Brook's relation overestimates the bond contraction and underestimates the E_B suppression because of the assumption of size-independent G and γ_0. Actually, the atomic vacancy should expand instead as the remaining bonds of the surrounding atoms contract. The strain of the entire nanoparticle arises from surface bond contraction and has little to do with the atomic void inside. One may note that E_B varies from site to site due to the difference of atomic CN environment at various locations of the solid.

14.2 Liquid–Solid Phase Transition

14.2.1 Undercooling: Skin Pre-Melting

Undercooling and overheating are the mostly attended activities of materials at the nanoscale. In many cases, surface liquidation and evaporation often occur at temperatures lower than the corresponding bulk values [14–16]. Likewise, liquid surface freezes at lower temperatures [17]. For substrate-supported nanosolids with relatively free surfaces, the T_m decreases with particle size (termed as undercooling). In contrast, as per the existing experimental evidence for embedded nanosolids, the T_m can be lower than the bulk T_m for some matrices. However, the same nanosolid embedded in some other different matrices may melt at temperatures higher than the bulk T_m (overheating). Overheating of 115 K occurs to Pb(111) films confined in an Al(111) matrix [18]. The T_m suppression for a free surface corresponds to the reduced degree of confinement and the increased entropy of the molecules at the surface compared with atoms in the bulk, whereas the T_m elevation or depression of the embedded nanosolids depends on the coherency between the nanosolids and the embedding matrix [19, 20].

There is an extensive database describing surface and nanosolid T_m suppression [21–26]. For instance, a photoelectron emission study [27] confirmed that lithium (110) surface melting occurs 50 K below the bulk T_m (454 K). A temperature-resolved XRD analysis revealed that the T_m of nanometer-sized drugs (polymer) also drops (by 33 and 30 K for 7.5-nm-sized griseofulvin and 11.0-nm-sized nifedipine, respectively) in a 1/R fashion [28]. STM measurements of a reversible, temperature-driven structural surface phase transition of Pb/Si(111) nanoislands indicates that the transition temperature decreases with inverse of domain size and the phase transition is independent of the processes of cooling or heating [29].

The T_m of a Pd nanowire is lower than the bulk value but higher than that of the cluster with countable number of atoms proceeding in a surface pre-melting manner. A quasi-liquid skin grows from the surface radially inward for both cluster and wire, followed by a breakdown of order in the remaining solid core at the transition temperature [30].

The size effect on the nanosolid melting has been modeled in terms of classical thermodynamics and atomistic MD simulations [31–46]. In general, the size-dependent T_m(K) follows the empirical scaling relationship:

$$\frac{\Delta T_m(K)}{T_m(\infty)} = -\frac{K_C}{K}, \tag{14.5}$$

where K_C is the critical size at which the nanosolid melts completely, or the $T_m(K_C) = 0$ K. The physics behind the K_C is the focus of modeling studies.

14.2.1.1 Classical Thermodynamics

Classical thermodynamics based on the surface Laplace and the Gibbs–Duhem equations [43] have derived that K_C obeys the following relations [41, 44]:

$$K_C = \frac{-2}{H_m(\infty)} \times \begin{cases} \sigma_{sv} - \sigma_{lv}(\rho_s/\rho 1)^{2/3}, & \text{(HGM)} \\ \sigma_{sl}(1 - K_0/K)^{-1} + \sigma_{lv}(1 - \rho_s/\rho 1), & \text{(LSM)} \\ [\sigma_{sl}, 3(\sigma_{sv} - \sigma_{lv}\rho_s/\rho 1)/2] & \text{(LNG)} \end{cases}$$

where H_m is the latent heat of fusion. ρ is the mass density and σ the interfacial energy. Subscripts s, l, and v represent the phases of solid, liquid, and vapor, respectively. The critical value of R_C (= $K_C d_0$) is normally several nanometers. These expressions correspond to three outstanding mechanisms in terms of classical thermodynamics:

1. The homogeneous melting and growth (HMG) model [32, 33] considers the equilibrium between the entire solid and the entire molten particle, which suggests that the melt proceeds throughout the solid simultaneously. This model describes well the case of smallest nanoparticle with K_C equal to three or less or otherwise to larger values with void defects being involved.
2. The liquid shell nucleation (LSN) model [34] assumes that a liquid layer of thickness K_0 is in equilibrium at the surface, which indicates that the surface melts before the core of the solid.
3. The liquid nucleation and growth (LNG) model [37, 38] suggests that melting starts by the nucleation of a liquid layer at the surface and moves into the solid as a slow process with a definite activation energy. The LSN and the LNG are valid to the melting of a flat surface or a larger nanoparticle.

14.2.1.2 Atomistic Models

Models based on atomistic/MD attribute the critical R_C to:

$$R_C = \begin{cases} 5{,}230\, v_0\gamma, & \left(v_0 = 4\pi d_0^3/3\right) \quad \text{(Liquid-drop)} \\ \alpha_m d_0, & (\alpha_m - \text{constant}) \quad \text{(Surf-phonon)} \\ R_0\left(\frac{1-\beta}{1-R_0/R}\right), & \quad \text{(Surf-RSMD)} \end{cases} \tag{14.6}$$

The liquid-drop model [47] relates the T_m to the E_{coh} of the entire particle of N atoms. With the involvement of surface, the E_{coh} equals the difference between the volume cohesive energy (NE_B) and the surface energy ($4\pi d_0^2 N^{2/3}\gamma$). The mean cohesive energy per atom with volume v_0 in the solid is $E_B(R) = E_B - E_{B,S}N^{-1/3}$, where $E_{B,S} = 4\pi d_0^2\gamma$ is the cohesive energy for an atom at the surface. The relation between the E_B and the $E_{B,S}$ is given empirically as, $E_{B,S} = 0.82\, E_B$ [48]. Based on the Lindemann's criterion of melting, the T_m of the bulk material follows [49],

$$T_m(\infty) = nf_e^2 E_B/(3k_B Z) \propto E_B \tag{14.7}$$

where n is the exponent of the repulsive part of the interaction potential between constituent atoms, Z is the valence of the atom, which is different from the atomic CN (z). The coefficient f_e is the thermal expansion magnitude of an atom at T_m. At T_m, the f_e is less than 5 % [50, 51]. The T_m depends simply on the mean atomic $\langle E_B(K)\rangle$ of the solid. Replacing the E_B with the size-resolved $E_B(K)$, Nanda et al. [47] derived the liquid-drop model for the $T_m(K)$ based on the relation:

$$E_b(\infty) = \eta_{1b}T_m(\infty) + \eta_{2b} \tag{14.8}$$

where the constant η_{2b} represents $1/z$-fold of the enthalpy of fusion and atomization, which is required for evaporating an atom from the molten state. η_{1b} is the specific heat per coordinate in the bulk. The η_{1b} and η_{2b} values are tabulated in Table 14.1 [47]. According to the liquid-drop notation, the critical radius at which $T_m(K_C)$ approaches 0 K is in the range of 0.34 (for Mn) and 1.68 nm (for Ga) [47].

The surface-phonon instability model [40, 52, 53] suggests that the $T_m(K)$ varies with $T_m(\infty)$ and with the energy for defect formation at the surface. Within the thermodynamic limit (particle radius larger than 2 nm), the effects of size reduction and electronic excitation combine [54].

The lattice-vibration instability model [40, 55–59] extends Lindemann's vibrational-lattice instability criterion [60]. The melting behavior of a nanosolid is related to the ratio (β) of the root-mean-square displacement (RMSD, δ^2) of an atom at the surface to the RMSD of an atom inside a spherical dot. β is a size-independent parameter:

$$\beta = \delta_s^2(D)/\delta_b^2(D) = \delta_s^2(\infty)/\delta_b^2(\infty)$$

The K_C is determined by $K_0 = \tau$ (dimensionality) at which all the constituent atoms have surface features. This model indicates that if $\beta > 1$, the surface melts below the bulk T_m, and vice versa. According to the RMSD, a nanosolid of $K_C = \tau$ radius will melt at 0 K.

14.2.2 Overheating: Interface Effect

In the case of embedded nanosolids, the coefficient of surface energy will be replaced by the interfacial energy if surfaces are completely saturated with atoms of the surrounding matrix. Nanda et al. [47] introduced the ratio as a perturbation of surface energy between the matrix and the embedded specimen,

$$\frac{\Delta T_m(K)}{T_m(\infty)} = -\frac{K_C}{K}\left(1 - \frac{\gamma_{Mat}}{\gamma}\right)$$

If the surface energy of the matrix $\gamma_{Mat} > \gamma$, the core nanosolid melts at a temperature that is higher than its bulk counterpart. This expression matches the experimental data of Pb particles embedded in an Al matrix but overestimates the T_m for Indium particles embedded in an Al matrix by some 10–20 K using the known γ and γ_{Mat} values.

Based on the size-dependent magnitudes of the atomic vibrations, Jiang et al. [40, 61] extended the T_m(K) model for the overheating, according to which overheating is possible if the diameter of the matrix atoms is smaller than the atomic diameter of the embedded nanosolid. Therefore, adjusting the β value in the *RMSD* model describes both overheating and undercooling of a nanosolid. Overheating happens when $\beta < 1$, which means that the matrix confines the vibration of the interfacial atoms.

However, MD simulations [62] suggest that atoms in the bulk interior of a freestanding nanosolid melt prior to the surface that melts at relatively higher temperatures. This prediction seems to be conflicting with existing database but as discussed shortly for the overheating of the smallest Ge^+ and Sn clusters. In contrast, MD calculations [63] of the melting evolution, atomic diffusion and vibrational behavior of bcc metal vanadium nanoparticles with diameters around 2–9 nm suggest that the melting proceeds in two stages. A stepwise pre-melting of the skin of two or three atomic layers happens first and then an abrupt melting of the entire cluster follows. The heat of fusion of nanoparticles is also inversely proportional to the nanoparticle size.

The models of LSN, HMG and LNG suit only the cases of T_m suppression ($\Delta T_m < 0$) while the liquid-drop and the RMSD models cover both the undercooling and the overheating. For particles larger than several nanometers, all the models worked sufficient well despite the disputable mechanisms.

14.2.3 BOLS Formulation

A Taylor's series of the binding energy of a pair of atoms can be decomposed as energies of binding at 0 K, $E_b(d_0)$, and the thermal vibration energy, $E_V(T)$:

$$\begin{aligned} E_{\text{total}}(r,T) &= \sum_n \left(\frac{d^n u(r)}{n!dr^n}\right)_{r=d_0} (r-d_0)^n \\ &= u(d_0) + 0 + \left.\frac{d^2u(r)}{2!dr^2}\right|_{d_0} (r-d_0)^2 + \left.\frac{d^3u(r)}{3!dr^3}\right|_{d} (r-d_0)^3 \cdots \\ &= E_{\text{b}}(d_0) + \frac{k}{2}(r-d_0)^2 + \frac{k\prime}{6}(r-d_0)^3 + \cdots \\ &= E_{\text{b}}(d_0) + E_{\text{V}}(T) = \begin{cases} 0, & (\text{Evaporation}) \\ E_{\text{C}}, & (Critical - T_{\text{C}}) \end{cases} \end{aligned} \tag{14.9}$$

The term of $n = 0$ corresponds to the minimal binding energy at $T = 0$ K, $E_{\text{b}}(d_0) < 0$. The term $n = 1$ is the force $[\partial u(r)/\partial r|_{d_0} = 0]$ at equilibrium and terms with $n \geq 2$ correspond to the thermal vibration energy, $E_{\text{V}}(T)$. The T_{C} can be any critical temperature for event such as liquid–solid, liquid–vapor, or other phase transition, like magnetic and ferroelectric transitions. By definition, the thermal vibration energy of a bond is,

$$\begin{aligned} E_{\text{V}}(T) &= \left.\frac{d^2u(r)}{2!dr^2}\right|_{d} (r-d)^2 + \left.\frac{d^3u(r)}{3!dr^3}\right|_{d} (r-d)^3 \cdots \\ &\cong \mu\omega^2 (r-d)^2 \Big/ 2 + 0[(r-d)^{n>2}] \\ &\approx k_{\text{v}} (r-d)^2 \Big/ 2 = \eta_1 T \end{aligned} \tag{14.10}$$

where $r - d_0$ is the magnitude of lattice vibration. μ is the reduced mass of a dimer of concern. The term $q_{\text{v}} = \mu\omega^2$ is the force constant for lattice vibration with an angular frequency ω.

The physical argument for the BOLS iteration is that, if one wishes to peel off or loosen an atom in the solid thermally, one must supply sufficient thermal energy to overcome the cohesion that binds the specific atom to its surrounding neighbors. The thermal energy required to loosen one bond is the separation of $E_{\text{b}}(T_{\text{C}}) - E_{\text{b}}(\text{T})$, see Sect. 14.2. If the $E_{\text{V}}(T)$ is sufficiently large, all the bonds of the specific atom will break and this atom will leave the solid. At the evaporating point of any kind of solid, $E_{\text{total}} = 0$; at the critical point, $E_{\text{total}} = E_{\text{C}}$. One may consider step-by-step the energies required for melting (or dissociating) a bond, an atom, and then shell-by-shell of a nanosolid of radius lined with K atoms.

The thermal energy required for loosening a bond of an atom in the bulk by raising the temperature from T to T_{C} equals,

$$E_T = E_{\text{b}}(T_{\text{C}}) - E_{\text{b}}(T) = \eta_1 (T_{\text{C}} - T) \propto E_{\text{b}}(0) \tag{14.11}$$

The energy required for melting the entire atom in a bulk is proportional to the $E_{\text{B}}(0)$, which is a sum of the single bond energy over all the coordinates.

Melting a nanosolid comprising N atoms in a shell-by-shell manner requires thermal energy that is proportional to the cohesive energy of the entire solid:

$$T_{\mathrm{m}}(K) \propto E_{\mathrm{coh}}(K) = N z_{\mathrm{b}} E_{\mathrm{b}} + \sum_{i \le 3} N_i (z_i E_i - z_{\mathrm{b}} E_{\mathrm{b}}) \tag{14.12}$$

If the bond nature in the solid is homogenous, the E_{coh} may vary from material to material, but for a specific sample, the fraction of the E_{coh} needed for the phase transition is fixed for a specific process occurring to the specimen [49]. The relative change in $T_m(K)$ and $T_C(K)$ is then:

$$\frac{\Delta T_{\mathrm{m}}(K)}{T_{\mathrm{m}}(\infty)} = \frac{\Delta T_{\mathrm{C}}(K)}{T_{\mathrm{C}}(\infty)} = \frac{\Delta E_{\mathrm{B}}(K)}{E_{\mathrm{B}}(\infty)} = \sum_{i \le 3} \gamma_i \left(z_{\mathrm{ib}} c_i^{-m} - 1 \right) = \sum_{i \le 3} \gamma_i (\alpha - 1) = \Delta_{\mathrm{B}} \tag{14.13}$$

The temperature is always the same throughout the specimen in operation whereas the intrinsic $T_{C,i}$ may vary from site to site if the sample contains atoms with different CN, such as atoms at the surface, grain boundary, or sites surrounding voids or stacking faults.

This mechanism explains why the latent heat of fusion of a solid has a broad range of measured values rather than appearing as a sharp peak [41, 64]. For a solid with numerous randomly distributed defects, the mechanism of random fluctuation melting [39] could dominate because energies required for breaking one bond or dissociating an individual atom with different CN are different. This mechanism also explains the broad temperature range for glass transition of an amorphous state as the random distribution of atomic CN imperfection in the amorphous solid. Glass transition happens in a range of temperatures and it is material processing condition dependent [65].

On the other hand, from a classical thermodynamic point of view, the thermal energy E_T required for the liquid–solid phase transition can be estimated by integrating the specific heat over the entire solid with and without CN imperfection from zero to the T_m:

$$\frac{\Delta E_T(K)}{E_T(\infty)} = \frac{\int_0^{T_{\mathrm{m}}(K)} C_{\mathrm{p}}(Kj, T)\mathrm{d}T}{\int_0^{T_{\mathrm{m}}(\infty)} C_{\mathrm{p}}(\infty, T)\mathrm{d}T} - 1 \cong \frac{\Delta T_{\mathrm{m}}(Kj)}{T_{\mathrm{m}}(\infty)} = \Delta_{\mathrm{B}} \tag{14.14}$$

with the assumption of $C_P(K, T) \cong C_P(\infty, T) \cong C_V(\infty, T) =$ constant in the entire temperature range [66]. It is true in fact that $C_P(K, T) \neq C_P(\infty, T) \neq C_V(\infty, T) \neq$ constant. The Debye temperature and therefore the specific heat C_P are size and temperature dependent [56, 67]. This effect results in a 3–5 % deviation of the C_P value. Besides, $(C_P - C_V)/C_V \sim 3$ % [66]. Compared with the precision in determining the size and shape of a nanosolid, such errors are negligible.

Actually, measurements [68–70] revealed that the C_P varies insignificantly with the particle size in the measuring temperature range. Therefore, it is acceptable to simplify the C_P as a constant in the integration. Such simplification may lead to slight deviation in the integration in Eq. (14.14) from the true value. Nevertheless, one should particularly note that the deviation of the integration from true value

only affects the precision of the m value or the effective z_{ib}, and it does not change the nature of the phenomenon.

14.2.4 Verification: Liquidation and Evaporation

Equation (14.13) indicates that the size-dependent $\Delta T_m(K)/T_m(\infty)$ originates from the relative change in the $E_{B,i}$ of a surface atom to the bulk value. The $\Delta T_m(K)/T_m(\infty)$ follows the scaling law given in Sect. 14.2. Figure 14.3 compares predictions using parameters given in Table 14.2 with the measured size-dependent melting behavior of metals, semiconductors, inert gases, and methyl chloride polymer (m-Cl), as well as embedded systems showing overheating effects. The size-dependent evaporating temperatures (T_{eva}) of Ag and CdS nanosolids also follow the trend of prediction.

The matching between BOLS prediction and measurements provides additional information about the mode of epitaxial crystal growth and the bonding status between the nanosolid and the substrate. Results show that Al nanosolids grown on a *SiN* substrate are more plate-like ($\tau = 1$) throughout the measured size but Sn on SiN and Au on C are more spherical-like ($\tau = 3$) at particle sizes smaller than 10 nm. The melting profiles show that at the smaller size range, Au/W interface promotes more significantly the melting of Au (undercooling) than the Au/C interface. The silica matrix causes a slight overheating of the embedded Au solid compared with the curves for Au on the other two substrates. The deviation from theory and experiment also provides information about the difference in interfacial energy between the particles and the substrates.

The BOLS premise indicates that the overheating of In/Al ($T_{m,In}/T_{m,Al} = 530/932$), Pb/Al (600/932), Pb/Zn (600/692), and Ag/Ni (1235/1726) [71] results from the interfacial bond strengthening. An atom performs differently at a free surface from this atom at the interface. Although the coordination ratio at the interfaces suffers little change ($z_{ib} \sim 1$), formation of the interfacial compound or alloy alters the nature of the interatomic bond that should be different in strength. In this case, one may replace the $z_{ib}C_i^{-m}$ with a parameter α to describe the interfacial bond enhancement, as indicated in panel (g).

Numerical fitting turns out the α value of 1.8, which indicates that an interfacial bond is 80 % stronger than the bond in the parent bulk. If one considers the bond contraction, 0.90 $\sim$ 0.92 [72], as the As and Bi impurities in CdTe compound, the m value is around 5.5–7.0. The high m value indicates that bond nature indeed evolves from a compound with m around four to a value of more covalent nature. Therefore, the deformed and shortened interfacial bond is much stronger. This finding means that electrons at an interface are deeply entrapped and densified. Therefore, it is understandable that twins of nanograins [73] and the multilayered structures [74] are stronger and thermally more stable.

It is anticipated therefore that a thin insulating layer could form in a heterojunction interface because of the interfacial bond nature alteration and the charge

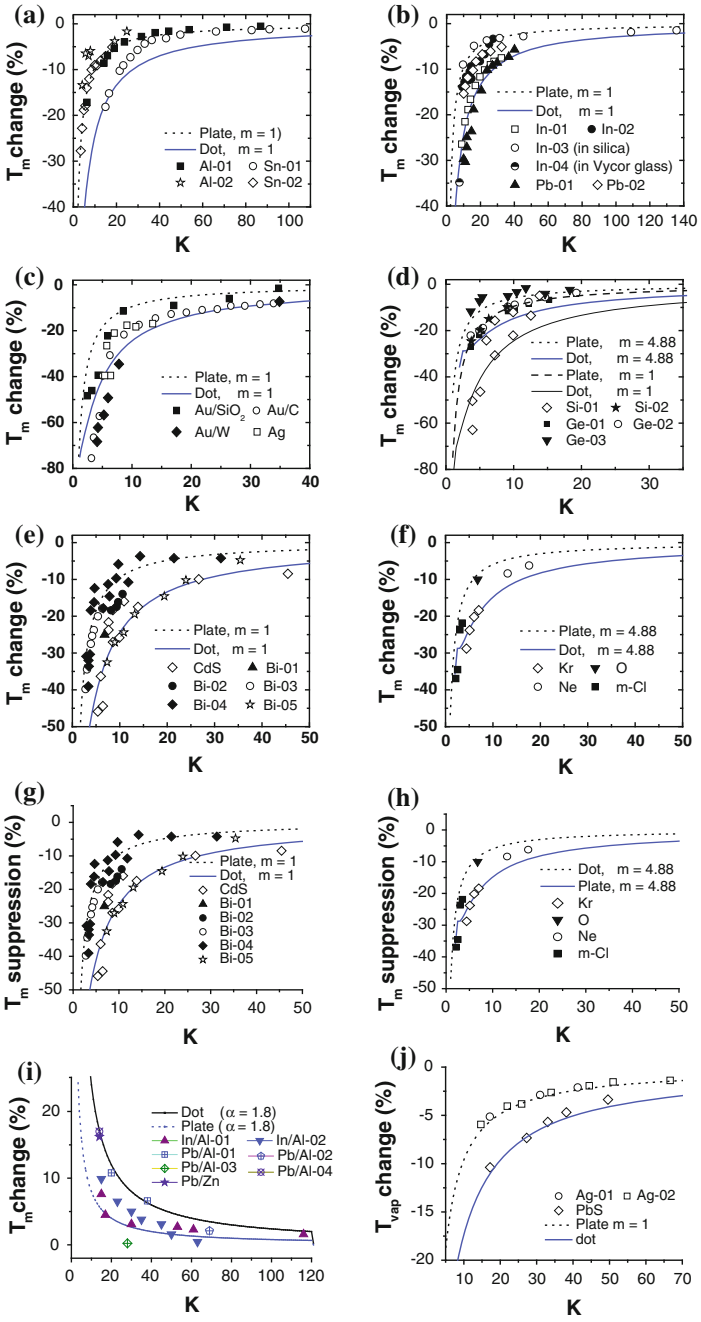

Fig. 14.3 Agreement between predictions (*solid lines*) and experimental observations of the size-and-shape dependence of the T_m suppression of **a** *Sn* and *Al* on Si_3N_4 substrate [66, 70], **b** In and Pd, **c** *Au* on *C* [33], W [32] and embedded in Silica [78], **d** Ge and Si, **e** Bi and CdS, **f** Kr, Ne and O, and m-Cl, **g** overheating of embedded In and Pb, **h** T_{eva} of Ag and PbS nanosolids [79]. Parameters and references are given in Table 14.2 (Reprinted with permission from [7])

Table 14.2 Parameters used in calculations presented in Fig. 14.3

Medium	$T_m(\infty)$	T_m intercept	Data sources (Ref.)
Al-01 (on SiN)	933.25		[69]
Al-02			[80]
Sn-01 (on SiN)	505.06		[81]
Sn-02			[82]
Au/C	1337.33		[33]
Au/SiO_2			[78]
Au/W		947	[32]
Ag	1,234		
In-01	429.76	438.9	[24]
In-02		433	[82]
In-03		443	[83]
Pb-01	600.6	632.6	[84]
Pb-02	600.6	607	[24]
Si-01	1,685	1,510	[85]
Si-02			[86]
Ge-01 (beginning)	930	910	[87]
Ge-02 (ending)	–	1023.3	
Ge-03 (recrystallization)		1260.8	
CdS	1,678	1,346	[14]
Bi-01	544.52		[24]
Bi-02		618.9	[82]
Bi-03		559.9	[88]
Bi-04		587.6	[89]
Bi-05		557.8	[90]
Kr	116	109.2	[91]
O	54.4		[92]
Ne	24.6		[85]
Methyl chloride (m-Cl)	175.6		[91]
In/Al-01	429.76	433	[93]
In/Al-02	429.76	423.8	[82]
Pb/Al-01	933.25	613.2	[19]
Pb/Al-02			[94]
Pb/Al-03			[95]
Pb/Al-04			[96]
Pb/Zn	692.73		[92]

T_m is the intercept of least-root-mean-square linearization of the experimental data that calibrate the measurements. Atomic sizes are referred to Appendix A2
For metals, $m = 1$. For embedded system, the $z_{ib}C_i^{-m}$ is replaced with a constant α that describes the bond strength enhancement due to the alloying at the interfaces

trapping effect. This anticipation explains the high interfacial stress (σ_P) of junction dislocations in aluminum [75] and provides new insight into the deformation of ultrafine-grained metals. The interface bond strengthening also explains the fact that a monolayer GaAs coating on a Ge(110) surface could raise the T_m (1211 K)

with an association of a dramatic drop of the diffusion coefficient of the Ge atoms. In contrast, a Ge monolayer coating on a GaAs(110) surface lowers the T_m of GaAs (1,540 K) by 300 K. Therefore, overheating is subject to the configuration of the hetero-junction interface and their respective $T_m(\infty)$ as well.

The T_m of Si and CdS nanosolids appeared to be lower than the expected values with $m = 4.88$ for Si. The reason of the deviation could be the definition of melting temperature that may refer to temperature of coalescence or complete melting. For instance, MD calculations revealed that [76] coalescence occurs at temperatures lower than the cluster T_m, and that the temperature difference between coalescence and melting increases with cluster size reduction. In the normalization of the scaling relation, the coalescence temperature is lower than the T_m and the coalescence T drops faster than T_m with solid size. The size-dependent T_m of Kr, Ne, and O solids follow the curve of m = 4.88 as well, despite the accuracy of measurement. The In particle encapsulated in silica exhibits overheating while the In embedded in Vycor glass shows no overheating effect. From the *RMSD* instability point of view, the interfacial binding constrains the *RMSD* of the interfacial atom to be smaller than that of a bulk atom [40].

Equation (14.13) indicates that the quantity $\alpha = z_i/z_b C_i^{-m}$ dictates the process of overheating ($\alpha > 1$, T_m elevation for chemically capped nanosolids) or undercooling ($\alpha < 1$, T_m suppression of freestanding nanosolids). For a capped nanosolid, $z_i/z_b \sim 1$, the α represents the interfacial bond strength. For a freestanding nanosolid, there are two possibilities for $\alpha > 1$. One is that the m increases as z_i is reduced and the other is that the C_i is much lower than the prediction [77].

14.2.5 T_m Oscillation

14.2.5.1 Observations

The hardness of a bulk material is proportional to its T_m. However, the skin of a solid is generally harder, but the melts more easily than the core interior. XRD in ultrahigh vacuum [44] reveals that the T_m of Pb nanosolids drops with crystallite size, which follows the liquid-skin melting mechanism. Such melting behavior is demonstrated via the reversible growth of a 0.5-nm (2 atomic diameters)-thick liquid skin on 50-nm-sized crystallites.

It is surprising, however, that a freestanding nanosolid at the lower end of the size limit, or clusters containing 10–50 atoms of Ga^+ or IV-A elements, melts at temperatures that are 10–100 % or even higher than the bulk $T_m(\infty)$ [29, 97–100]. For example, Ga^+_{39-40} clusters melt at about 550 K, while a $Ga^+{}_{17}$ cluster does not melt even up to 700 K compared with the $T_m(\infty)$ of 303 K [97]. Small Sn clusters with 10–30 atoms melt at least 50 K above the $T_m(\infty)$ of 505 K [22]. Numerical optimizations suggest that $Ga^+{}_{13}$ and $Ga^+{}_{17}$ clusters melt at 1,400 and 650 K [98]

and Sn_n (n = 6, 7, 10 and 13) clusters melt at 1,300, 2,100, 2,000, and 1,900 K, respectively [100]. For a Sn_{10} cluster, the structural transition happens at 500 and 1,500 K and the structural transition of a Sn_{20} cluster occurs at 500 and 1,200 K [101]. The Sn^+_{10} and $Sn^+{}_{11}$ clusters survive up to 1,073 K while Sn clusters containing $n > 19$ and $n < 8$ atoms are less thermally stable as melting occurs at 773 K or below [102]. Sn_{19} can remain solid up to 673 K while Sn_{20} melts below 673 K.

Calculations [99] suggested that the IV-A elements, C_n, Si_n, Ge_n, and Sn_n ($n \sim 13$) clusters melt at temperatures higher than their $T_m(\infty)$. The measured T_m for Bi particles of 7 nm in radius was similar, being up to 50 K above the value predicted by the homogeneous melting model [103]. The C_{13} cluster prefers a monocyclic ring or a tadpole structure, which is most probable to appear in the simulated annealing when the temperature is between 3,000 and 3,500 K. Numerical calculations, suggested that at the smallest sizes, carbon atoms tend to form tubes or fullerene rather than tetrahedron diamond. Although the T_m may be overestimated to some extent for the smallest clusters [100], the calculated T_m elevation follows the trend of measurement.

The T_m elevation of the smallest Ga and Sn nanosolid corresponded either to the bond nature alteration from covalent-metallic to pure covalent with slight bond contraction [98, 104], or to the significant geometrical reconstruction as Ge, Si, and Sn clusters are found to be stacks of stable tricapped trigonal prism units [105].

14.2.5.2 BOLS Formulation

The generality of the atomic clusters is the atomic CN that is one or two lower than the atomic CN at a flat surface, four. As demonstrated in Sect. 14.3, only one CN loss makes a great difference—the bond is much shorter and stronger than the bonds at the surface.

The T_m oscillation over the whole range of sizes for Sn and Ga^+ clusters can be formulated by varying the bond nature index m as a function of z. Optimization leads to the relation that expresses the m value over the range from seven at $z = 2$ to one at $z > 4$:

$$m(z) = 1 + 12/\{1 + \exp[(z - 2)/1.5]\}$$

Figure 14.4 shows that the T_m curves drop generally with size and then bends up at $K > 3$ ($\mathrm{Log}(K) > 0.5$, or $z > 3$) for higher m values. If the T_m rise originates from the C_z deviation without bond nature change, the bond will contract to $C_z = 0.7^7 = 0.082$. A 92 % bond contraction is impossible. Therefore, the m value, or the bond nature, must change with CN for these elemental solids. As the smallest clusters are not spherical in shape, the equivalent size might be subject to adjustment.

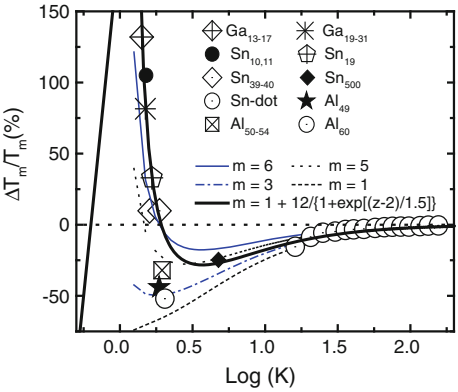

Fig. 14.4 Comparison of the predicted T_m ossification with those measured from Ga^+_{13-17} [91, 97], Sn^+_{10-19} [102], Sn^+_{19-31} [22], Ga^+_{39-40} [97], Sn_{500} [112], and Sn nanosolid on Si_3N_4 substrate [64]. The T_m deviation of Al^+_{50-60} clusters [109] from the predictions indicates that the bond nature alteration of Al is less significant compared to Sn and Ga bonds. Ideal fit is reached with a function of $m(z) = 1 + 12/[1 + \exp(z - 2)/1.5]$ to let m transit from 7 at $z = 2$ to 1 when $z > 4$ [113]

The $m(z)$ modification matches closely the measurement of $Ga^+{}_{17}$, $Ga^+{}_{39-40}$, Sn_{19-31}, and Sn_{500} clusters, and Sn nanosolids deposited on Si_3N_4 substrate as well [64]. Calculations [100] show that the T_m transition for Sn_{6-13} happens at Sn_7. Results indicate that the nature of the Sn–Sn and the Ga–Ga bond indeed evolves from metallic covalent to pure covalent as atomic CN reduces to much lower values, as expected by Chacko et al. [98].

This bond nature evolution also complies with findings that the Al–Al bond for under-coordinated or distorted Al atoms at grain boundaries [106] and at free surfaces [107] becomes shorter ($\sim$5 %) and stronger with increasing covalent character [108]. However, bond nature evolution in $Al^+{}_{49-60}$ clusters appears not as significant as occurred in Sn and Ga, as the T_m for $Al^+{}_{49-63}$ is 300 K lower than the $T_m(\infty)$. The abrupt T_m rise ($\sim$180 K) for $Al^+{}_{51-54}$, $Sn^+{}_{10-11}$ and $Sn^+{}_{19-20}$ clusters [109] may be partly due to the closed shell structures that are highly thermally stable [110, 111].

Results show that bonding to two neighbors is stronger for an IV-A atom than bonding with three or more due to the bond nature evolution. This mechanism explains why a C_{13} cluster prefers a ring or a tadpole structure with each atom having two bonds, or tubes, or GNR sheet, or fullerene having three neighbors rather than the densely packed tetrahedron structure of four neighbors [99]. For the covalent, Si ($m = 4.88$) and C ($m = 2.56$) clusters should also show the T_m elevation (bending up) at $K < 3$ with fewer than four neighbors.

The bond nature evolution may be the unique property of the III-A and IV-A elements with a larger number of electrons as compared to Al (m $\sim$ 2), Ga (m = 6–7), C ($m = 2.56$), Si ($m = 4.88$), and Sn (m = 6–7).

14.2.6 Remarks

The BOLS premise has reconciled the undercooling, overheating, and oscillating of the T_m over the whole range of sizes of various specimens to the effect of atomic CN imperfection and bond nature alteration. Atomic CN revised cohesive energy of the under-coordinated system determines the geometrical reconstruction, surface lattice/phonon instability, and surface energy. Actually, the surface and interfacial energy, surface stress, the local mass density of liquid and solid are all functions of atomic separation and bond energy that are subject to the BOLS correlation.

The T_m suppression is directly related to the atomic CN imperfection and its effect on the bond strength. The T_m elevation of embedded system is related to the strengthening of the interfacial bond. The T_m oscillation over the whole range of size of III-A and IV-A elements results from atomic CN variation and bond nature evolution.

14.3 Solid Phase Transition

14.3.1 Observations

With reduction in a solid size, the phase stability of the solid becomes lower as well. The T_C of ferromagnetic [114–116], ferroelectric [117–119], and superconductive [120–122] nanosolids can be modified by adjusting the shape and size of the nanosolid. The tunable T_C will be an advantage for sensors or switches that can be functioning in a designed temperature range.

14.3.1.1 Ferromagnetic T_C

For ferromagnetic nanosolids, such as Fe, Co, and Ni and their alloys or compounds [123–125], the T_C reduces with the particle size or with the thickness of the films [114, 116, 126–133]. The T_C of Prussian blue nanowire is also reduced with respect to the bulk [134] due to the diminution of the average number of nearest magnetic neighbors and magnetic exchange interaction constants. According to the scaling theory [135], a spin–spin correlation length (SSCL, or ξ) limitation model [136, 137] defines the SSCL as the distance from a point beyond which there is no further correlation of a physical property associated with that point. Values for a given property at distances beyond the SSCL are purely random. The SSCL depends functionally on temperature as $\xi = \xi_0(1 - T/T_C)^{-\nu}$, with ν being a universal critical exponent. The SSCL premise indicates that the ξ is limited by the film thickness. If the ξ exceeds the film thickness K, the T_C will be lower than the bulk value. The SSCL mechanism gives rise to the power-law form of $T_C(K)$ that

involves two freely adjustable parameters, λ and C (or C_0). The λ value varies from unity to 1.59 for the mean-field approximation and the three-dimensional Ising model, respectively [127, 135, 137]:

$$\frac{\Delta T_C(K)}{T_C(\infty)} = (C_0 K)^{-\lambda} \tag{14.15}$$

An alternative non-continuous form based on the mean-field approximation covers the thinner scales [138]:

$$\frac{\Delta T_C(K)}{T_C(\infty)} = \begin{cases} -\left(\frac{\xi+1}{2Kj}\right)^{\lambda}, & (K > \xi) \\ \frac{K-1}{2\xi} - 1, & (K < \xi) \end{cases} \tag{14.16}$$

This relation shows that T_C varies linearly with K and approaches to zero at $K = 1$ (single atom). If $\lambda \neq 1$, there is a discontinuity at $K = \xi$.

The T_C change in a spherical nanosolid is often related to the counts of surface bonds [139]. If the number of exchange bonds per unit volume inside the bulk is z, the number of bonds for the magnetically active surface atom is $z/2$ or less. The T_C is proportional to the mean number of exchange bonds per unit volume, and then, the relative change in the T_C is:

$$\frac{\Delta T_C(K)}{T_C(\infty)} = -\frac{\tau \Delta K}{2K} \tag{14.17}$$

where ΔK is the thickness of the layer with half-depleted exchange bonds. The quantity ΔK is an average that characterizes the features of the surface CN-deficient structure of a nanosolid. If ΔK is independent of the particle radius K, the T_C drops with K and the critical K_C at which T_C is zero is $\tau \Delta K/2$. This relation characterizes qualitatively the interrelation between the degree of magnetic structure disorder and the particle size for Fe_3O_4 spherical dots [140] by setting the critical thickness ΔK of half (for larger size) and two (for the smallest size) atomic sizes.

14.3.1.2 Superconductive T_C

Highly dispersed superconducting nanosolids can be coupled due to the proximity effect when the interparticle spacing is of the order of twice the penetration length of the superconducting order parameter in the normal phase [141, 142]. The electronic energy levels of the sample are discrete, with a mean-level spacing of Kobo gap δ_K for fine metallic particles [143, 144]: $\delta_K = 4E_F/3n \propto 1/V \propto K^{-3}$. As pointed out by Anderson [145], superconductivity would not be possible when δ_K becomes larger than the bulk E_G. Thus, the relation between the superconducting phase transition and the energy-level spacing for spherical granules follows the relation [146, 147]:

$$Ln\left(T_C(Kj)/T_C(\infty)\right) = \sum \left[2/\left(2m_j+1\right)\right] \times \left[\tanh\left[(\pi/2)\left(\left(2m_j+1\right)2\pi k_B T_C/\delta_K\right)\right] - 1\right]$$

Index m_j is the magnetic quantum number. Estimation using this relation yields a 2.5 nm critical size for the disappearance of superconductivity of Pb nanosolid. Experiments of Giaver and Zeller [122] on Sn confirmed the existence of a metastable energy gap only for particles larger than 2.5 nm. However, the T_C for Pb is detectable when the grown Pb atomic layers on Si substrate are four and more [148]. The T_C suppression of Pb embedded in the Al-Cu-V matrix [121] does not follow this relation but the following:

$$T_C(K) = T_C(\infty)\exp(-K_C/K)$$

with $T_C(\infty) = 7.2$ K for Pb [120]. Due to the finite number of electrons in each particle (between 1,000 and 64,000 depending upon the grain size), the conventional BCS approach loses its validity because the bulk BCS theory of superconductivity assumes an infinite number of electrons. Small size implies fewer electrons at the Fermi surface and the increased separation of Kubo levels. Additionally, energy-level spacing may be larger compared to thermal energy $k_B T$. Therefore, the assumption of metallic behavior of these particles is subject to examination.

The T_C of superconductive MgB_2 thin films decreases and the residual resistance increases when the epitaxial MgB_2 thin films become thinner [120, 149]. At sizes larger than 300 nm, the T_C saturates at 41.8 K. The resistivity also saturates to the bulk value of 0.28 Ω cm at 300 nm. A possible explanation of higher T_C is the strain in the film, while the grain size is not likely to be the direct cause of the thickness dependence of T_C. XRD revealed that the a lattice expands from the bulk value of 0.3086 to 0.3095 nm while the c lattice contracts from 0.3524 to 0.3515 nm for a 230-nm-thick MgB_2 film [150]. Hur et al. [151] reported a higher-than-bulk T_C in MgB_2 films on boron crystals and suggested that it is due to tensile strain. A T_C elevation is possible by compressing the c-axis [152]

14.3.1.3 Ferroelectric T_C

Unlike ferromagnetic and superconductive nanosolids that show smaller critical sizes for $T_C = 0$ K, a ferroelectric nanosolid often shows larger critical size at which the ferroelectric feature disappears [153]. Reducing the grain size from 1,200 to 50 nm results in a progressive reduction in tetragonal distortion, heat of transition, T_C, and relative dielectric constant of $BaTiO_3$ crystal [154]. The critical size for ferroelectricity disappearance is in the range of 10–30 nm. A combination of the size effect and the size-dependent 'dilution' effect of a grain boundary 'dead' layer could be the cause depressing the relative permittivity. The remnant polarization of the nanoscaled Pb(Zr, Ti)O_3 thin films decreases from 6.0 to 2.5 μC/cm^2,

while the coercive field increases from 50 to 150 kV/cm, with the decrease in film thickness from 152 to 32 nm [155].

Theoretical approaches for the ferroelectric depression include: (1) pseudospin theory based on the Ising model in a transverse field, (2) macroscopic Landau theory with consideration of surface effects, and (3) a polaron model for the very-long-wavelength region. The Landau-type model of Zhong et al. [156] considers the surface and non-equilibrium energy by introducing a surface extrapolation length δ to the size-depressed T_C of ferroelectric nanosolids, expressed using the Ising premise, $J_{ij} = J/r_{ij}^{\sigma}$. $\sigma = 0$ corresponds to an infinite-range interaction and $\sigma = \infty$ to a nearest-neighbor interaction [157].

Bursill et al. [158] assumed that the Landau-Ginzburg-Devonshire (LGD) coefficients in the Gibbs energy change with particle size. Huang et al. [159] combined the LGD theory and the BOLS correlation to study the size effect of ferroelectrics. The model assumes that the surface bond contraction is the origin for the size effect [160], which was confirmed by measurements. For example, barium titanate particles consist of a shell of cubic material surrounding a core of tetragonal material [161–163].

The following scaling relation is widely used to fit the T_C suppression of ferroelectric nanosolids [118],

$$\Delta T_C(K)/T_C(\infty) = C/(K - K_C) \tag{14.18}$$

where C and the K_C are adjustable parameters. The proper form of the dividend seems to be $K + K_C$ instead of $K = K_C$. Jiang et al. [164] adopted their model for T_m suppression to the size-dependent T_C of the ferroelectric nanosolids as:

$$\begin{cases} T_C(K)/T_C(\infty) = \exp\left\{-2S_0[3R_S(K/K_C - 1)]^{-1}\right\} \\ K_C = \alpha_{90}\left(2k_B\alpha\beta^2\right)^{-1} \end{cases}$$

where S_0 is the transition entropy and R_S is the ideal gas constant. α is the thermal expansion coefficient and β the compressibility. The constant α_{90} denotes the density of 90° domain walls. This relation reproduces the measured T_C suppression of $BaTiO_3$ and $PbTiO_3$ nanosolids with the known S_0 values.

14.3.1.4 Antiferromagnetic Transition

When a sufficiently large magnetic field is applied along the preferred axis, the so-called spin-flop reorientation occurs, i.e., a 90° rotation of the sublattice vectors, in the antiferromagnetic α-Fe_2O_3 nanosolids [165]. Both the spin-flop field, $H_{S\text{-}F}$ ($T = 0$), and the Morin transition temperature (T_M) decrease with particle size in a K^{-1} way and approach to zero when the diameter is smaller than 8 nm, for spherical particles [166]. Table 14.3 features the size-dependent $H_{S\text{-}F}$ and T_M values.

Table 14.3 Size dependence of the Morin temperature (T_M) and the spin-flop transition field at $T = 0$ ($H_{S\text{-}F,0}$) for the heminatite nanosolids [165]

D/nm	T_M/K	$H_{S\text{-}F,0}$/Tesla
36.4	186	1.7
40.0	200	2.5
82.7	243	5.4
159.0	261	6.6

The CN of the surface spins determines a variety of reversal paths and in turn affects both the exchange and anisotropy fields [165]. Therefore, the surface spins undergo spin-flop instability at field that is much lower than the field for the bulk. For Ho films, the helical antiferromagnetic ordering temperature, called Néel temperature (T_N), decreases with film thickness [167]. The offset thickness is 11 ML for metallic Ho films in comparison with the value of 16 ML for Cr in sputtered, epitaxial Fe/Cr(001) superlattice [168]. In the $Pr_{0.5}Ca_{0.5}MnO_3$ nanowires, a ferromagnetic transition occurs at $\sim$105 K; the antiferromagnetic transition happens at 175 K; and the charge ordering transition is suppressed from the bulk value of 245 K [169].

14.3.2 BOLS Formulation

An extension of the BOLS correlation into the Ising model could improve the insight into size-induced T_C suppression of ferromagnetic, ferroelectric, and superconductive nanosolids as well as the T_M and $H_{S\text{-}F}$ for antiferromagnetic heminatite.

14.3.2.1 Ising Model

The Hamiltonian of an Ising spin system in an external field B is expressed as [138],

$$H_{ex} = \sum_{\langle i,j \rangle} J_{ij} S_i S_j - g\mu_B B \sum_{i=1}^{N} S_i \propto z_i d_i^{-1}$$

The H_{ex} is identical to the atomic E_B under zero external field, $B = 0$. S_i and S_j is the spin operator in site i and site j, respectively. J_{ij} is the exchange strength between spins, which is inversely proportional to atomic distance. The sum is over all the possible coordinates, z_i. For phase transition, the thermal energy required is in equilibration with a certain portion of the exchange energy. This mechanism leads to the case being the same as for T_m suppression as described in Eq. (14.13).

14.3.2.2 High-Order CN Imperfection: The Dual-Shell Model

For ferroelectric systems, the exchange energy also follows the Ising model, but the S_j here represents the quanta of a dipole or an ion (called quasi-dipole) that is responsible for the ferroelectric performance. The difference in the correlation length is that the dipole system is longer than that of a ferromagnetic spin–spin system. Usually, dipole–dipole Van der Vaals interaction follows the r^{-6} type whereas the superparamagnetic interaction follows an r^{-3} relation. Hence, it is insufficient to count only the exchange bonds within the nearest neighbors for atoms with distant interaction in a ferroelectric system.

A dual-shell model describing the short- and the long-range interactions in the ferromagnetic nanosolid is necessary [170]. A critical exchange correlation radius K_C can be defined to count contributions from all atoms within the sphere of radius K_C. Therefore, the sum in Eq. (14.13) changes from the z_i neighbors to atoms within the K_C-sized correlation volume.

For a ferroelectric spherical dot with radius K, one needs to consider the interaction between the specific central atom and its neighbors within the critical volume $V_C = 4\pi K_C^3/3$, in addition to the BOLS correlation limited to the skin. The ferroelectric property drops down from the bulk value to a value smaller than 5/16 (estimated from Fig. 14.5) when one goes from the central atom to the edge along the radius. If the surrounding volume of the central atom is smaller than the critical V_C, the ferroelectric feature of the central atom attenuates; otherwise, the bulk value remains. For an atom in the ith surface layer, the number of the exchange bonds loss is proportional to the volume V_{vac} that is the volume difference between the two caps of the V_C-sized sphere as illustrated in Fig. 14.5a. Therefore, the relative change in the ferroelectric exchange energy of an atom in the ith atomic layer to that of a bulk atom due to volume loss becomes,

$$\frac{\Delta E_{exc,i}}{E_{exc}(\infty)} = \frac{V_C - V_{vac,i}}{V_C} - 1 = -\frac{V_{vac,i}}{V_C} = \delta_{V,i} \tag{14.19}$$

14.3.2.3 Generalization of T_C Suppression

Considering the BOLS correlation for the nearest neighbors and the volume loss of long-order CN imperfection, we have a generalized form for the T_C suppression for the ferromagnetic, ferroelectric, and superconductive nanosolids ($m = 1$ in the Ising model):

$$\frac{\Delta T_C(K)}{T_C(\infty)} = \frac{\Delta E_{exc}(K)}{E_{exc}(\infty)} = \begin{cases} \sum_{i \le 3} \gamma_i \left(z_{ib} C_i^{-1} - 1 \right) = \Delta_B & \text{(short-order-loss)} \\ \sum_{i \le K_C} \gamma_i \delta_{V,i} + \Delta_B = \Delta_{COH} & \text{(long-order-loss)} \end{cases} \tag{14.20}$$

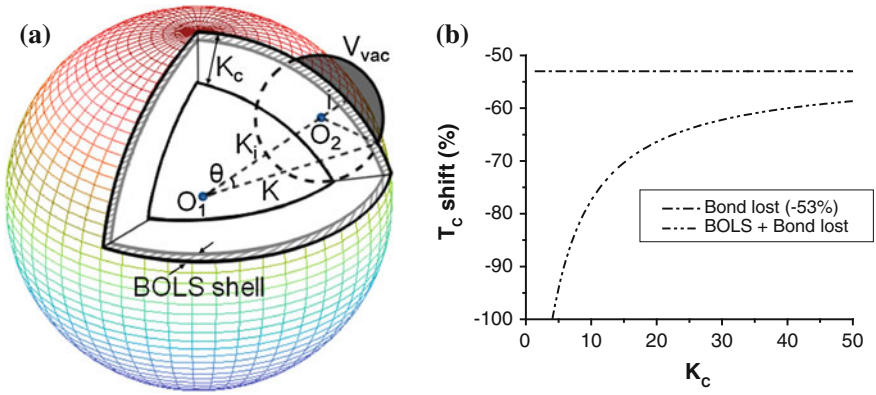

Fig. 14.5 The dual-shell model for the short- and long-range interactions in nanosolid ferroelectric nanosolid. **a** Schematic of the high-order exchange bonds loss of an atom in a spherical nanosolid with radius K. K_C is the critical correlation radius. The V_{vac} loss (the shaded portion) is the difference between volumes of the two spherical caps: $V_{vac,i} = \pi(K_C + K_i - K\cos\theta)^2(K_C - \frac{K_C+K_i-K\cos\theta}{3}) - \pi(K - K\cos\theta)^2(K - \frac{K-K\cos\theta}{3})$, where the angle θ is determined by the triangle O_1O_2A. **b** Correlation radius K_C dependence of the T_C shift of ferroelectric and superconductive nanosolids. For $K_C = 5$ example, BOLS lowers the T_C by -41.1 %, the high-order bond loss contributes to the T_C suppression by -53 %, and the overall T_C shift is -94 %. $K_C \leq 4$, $T_C = 0$ [171] (Reprinted with permission from [7])

For a short-order spin–spin interaction, the sum is over the outermost three atomic layers in terms of BOLS whereas for a long-order dipole–dipole interaction, the sum is within the sphere of the critical volume V_C. Therefore, ΔK in Eq. (14.17) is not a constant. In the BOLS premise, the γ_i is not always proportional to the inverse radius, which drops instead from unity to infinitely small when the particle grows from atomic scale to macroscopic size. Meanwhile, the z_i and the C_i vary with the curvature of the sphere.

Figure 14.5b shows the general K_C dependence of the ferroelectric T_C shift involving both the volume loss and the BOLS effect. For $K_C = 5$ example, bond contraction lowers the T_C by -41.1 % and the volume loss lowers the T_C by -53 % and the overall T_C shift is -94 %.

14.3.3 Verification: Critical Size

Least-root-mean-square linearization of the measured size-dependent T_C represented by Eq. (14.20) gives the slope B′ and an intercept that corresponds to the bulk $T_C(\infty)$. The $B' = K\Delta_{COH}$ for a ferroelectric system. For a ferromagnetic system, $B' = K\Delta_B$ is a constant without needing numerical optimization. Calculations based on Eq. (14.20) were conducted using the average bond length (appendix A2) and the known $T_C(\infty)$ values listed in Table 14.4.

Table 14.4 BOLS predicted critical correlation radius (K_C) in comparison with the documented R'_C of magnetic, ferroelectric, superconductive, and antimagnetic nanosolids

Materials	$T_C(\infty)$/K	K_C/R_C(nm)	R'_C/nm (Ref.)
Fe	1,043	1	0 [116]
Co	1,395	1	0 [114]
Ni	631	1	0 [114]
Fe_3O_4	860	1	0 [140]
$PbTiO_3$	773	4/1.04	6.3 [118], 4.5 [117]
$SrBi_2Ta_2O_9$	605	4/1.0	1.3 [119]
$PbZrO_3$	513	8/2.3	15 [174]
$BaTiO_3$	403	100/24.3	24.5 [177], 55 [173]
MgB_2	41.7	3.5/1.25	1.25 [175]
Pb	7.2	3.5/1.25	1.25 [121]

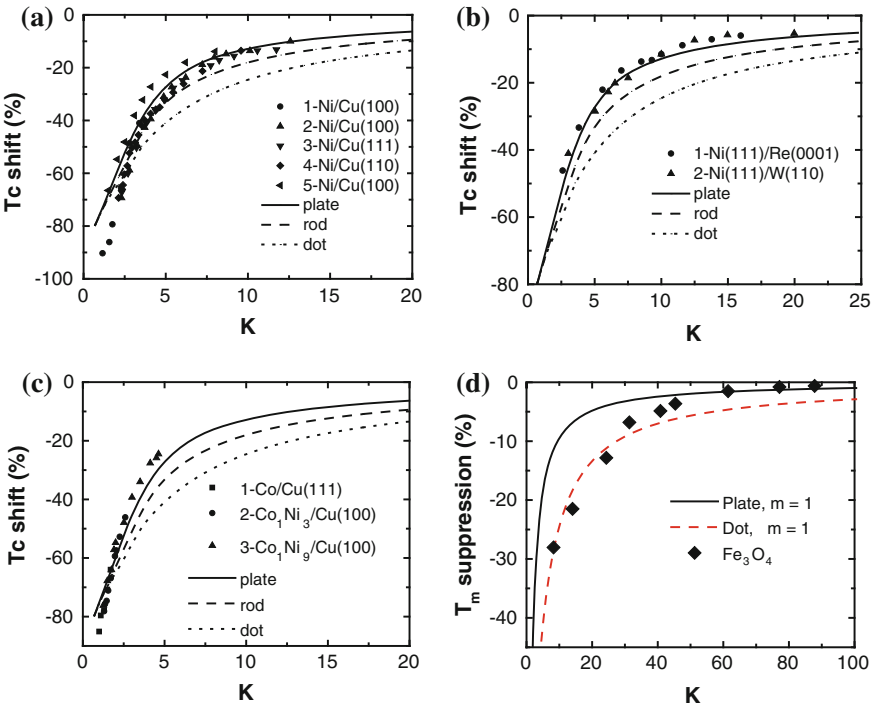

Fig. 14.6 Comparison of the predicted T_C suppression with observations of **a** Ni thin films: data 1 [130], data 2, 3, and 4[138], data 5[114], **b** data 1[172] and data 2 [129], **c** Co films [114], and **d** Fe_3O_4 nanosolids [140] (Reprinted with permission from [7])

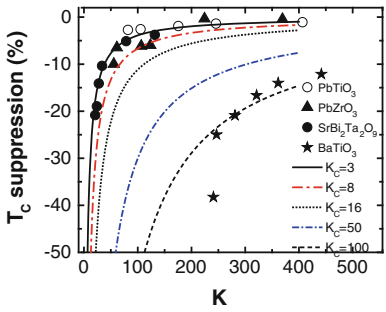

Fig. 14.7 T_C suppression of ferroelectric $PbTiO_3$ [117], $SrBi_2Ta_2O_9$ [119], $BaTiO_3$ [173], and antiferroelectric $PbZrO_3$ [174] nanosolids with different K_C values (Reprinted with permission from [7])

Figure 14.6 shows the T_C suppression for ferromagnetic Ni, Co, and Fe_3O_4 nanosolids. For ultrathin films, the measured data are closer to the predicted curve for a spherical dot. This coincidence indicates that at the beginning of film growth, the films prefer island patterns that transform gradually into a continuous slab. For a ferroelectric system, we need to optimize the K_C value by in computation to match theoretical curves to the measured data.

Figure 14.7 shows the T_C suppression of ferroelectric $PbTiO_3$ [117], $SrBi_2Ta_2O_9$ [119], $BaTiO_3$ [173], and antiferroelectric $PbZrO_3$ [174] nanosolids. For ferroelectric and superconductive nanosolids, $T_C = 0$ K occurs at $V_{vac} = V_C$, which means that K_C corresponds not to $T_C = 0$ K, but to a value that is much lower than room temperature. The difference in the optimized K_C by different approaches, as compared to Table 14.4, lies in that the γ_i is not a constant but changes with particle size.

Comparing the BOLS prediction to the measured T_C suppression of superconductive MgB_2 nanosolids in Fig. 14.8 leads to an estimation of the critical radius $K_C = 3.5$ of measurement ($R_C \sim 1.25$ nm) [175]. For the smallest MgB_2 crystals, the relative Bragg intensities of the allowed reflections can only match during Rietveld refinement by introducing statistically distributed B-vacancies, with the refined value falling from 1 to 2/3. This fact means that the average CN of Mg to B atoms falls from 12 to 8, which indicates the loss of superconductivity due to the under-coordination effect [176]. Therefore, long-range interaction is important to the superconductive T_C. For an Al–Cu–V embedded Pb nanosolid [121], the K_C is around 1, being the same to the ferromagnetic solid. For the antiferromagnetic α-Fe_2O_3, a spin-flop transition at a critical size of 8 nm results also from the high-order CN imperfection. Therefore, the long-order interaction dominates the T_C for all the ferroelectric, antiferroelectric, and superconductive nanocompounds.

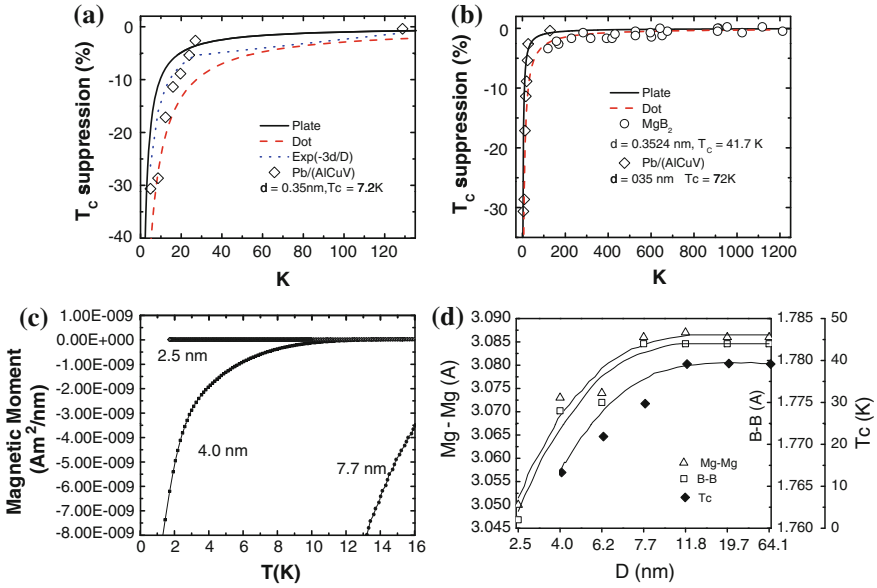

Fig. 14.8 Superconductive T_C suppression of **a** Pb particles embedded in Al-Cu-V matrix [120]. **b** MgB_2 films [120]. **c** Size and temperature dependence of the magnetism of MgB_2 superconducting nanosolids. **d** Size-induced T_C and bond length suppression of MgB_2 nanosolids [175] (Reprinted with permission from [7])

14.4 Diffusion and Crystal Growth

14.4.1 Diffusivity

14.4.1.1 Observations

The kinetics of diffusion occurring in nanostructured materials is a subject of intensive study [178, 179]. Materials at the nanoscale showed sharp acceleration of diffusion [180], indicating the lowered activation energy of diffusion. The activation enthalpies for the interfacial diffusion are comparable to those for surface diffusion, which are much lower than those for diffusion along grain boundaries [181, 182].

Measuring grain boundary diffusion fluxes of Cu and creep behavior of coarse-grained and nanostructured Ni samples at 423 and 573 K [183] revealed that the creep acceleration behavior is grain size-dependent because of the high diffusivity in the finer grain material. Fe-tracer diffusion in submicrocrystalline Pd powders demonstrates that interfacial diffusion occurs at relatively low temperatures accompanied by a substantial recovery of grain growth [184]. Atomic defects trigger the recovery processes and the crystal growth occurring in a main recovery stage at 500 K. The under-coordinated atoms surrounding the defects are

responsible for the onset of diffusion in the interfaces as these atoms are mobile in this temperature regime.

By means of surface mechanical attrition treatment (SMAT) to a pure iron plate, Wang et al. [185] fabricated a 5-μm-thick Fe surface layer composed of 10–25-nm-sized grains without porosity or contamination on the Fe plate. They measured Cr diffusion kinetics within a temperature range of 573–653 K in the nano-Fe-coated plate. The diffusivity of Cr in the nanocrystalline Fe is 7–9 orders higher in magnitude than that in a Fe lattice and 4–5 orders higher than that in the grain boundaries (GBs) of α-Fe. The activation energy (E_A) for Cr diffusion in the Fe nanophase is comparable to that of the GB diffusion, but the pre-exponential factor is much higher. The enhanced diffusivity of Cr in Fe corresponded to a large volume fraction of non-equilibrium GBs and a considerable amount of triple junctions in the presence of the nanocrystalline Fe samples.

Under the given conditions, copper atoms were not detectable in the coarse-grained Ni even at a depth of 2 μm. However, the diffusive copper fluxes in nanostructured Ni penetrate into a depth greater than 25 and 35 μm at 423 and 573 K, respectively [183]. This information leads to the GB diffusion coefficients of copper in nanostructured nickel as derived as follows.

As no migration of the GBs in nanostructured Ni was observed at 423 K, the diffusion coefficient, D_b, can be determined using the equation describing the change in the GB impurity concentration versus time t of the diffusion at annealing [186]:

$$c(x,t) = c_0 \mathrm{erfc}\left[x/\left(2\sqrt{D_b t}\right)\right]$$

where c_0 is the concentration of copper in the skin. The depth x is the distance from the surface at which $\log c = -1$ ($c = 0.1$ %, which corresponds to the resolution limit of the SIMS unit). An extrapolation of the experimental concentration curve at $x \to 0$ gives the value of c_0. In this case, $D_b = 1 \times 10^{-14}$ m^2/s ($t = 3$ h).

Grain growth occurs in nanostructured nickel annealed at 573 K, and the grain boundary migration occurs at the velocity of $V \sim 7 \times 10^{-11}$ m^2/s. In this case, the D_b follows [186]:

$$c(x,V,\beta) = c_0 \exp\left(-x\sqrt{V/D_b\beta_b}\right)$$

Considering the diffusion width of the boundary $\beta_b = 10^{-8}$ m, one can obtain the $D_b = 1.4 \times 10^{-12}$ m^2/s, which is two orders higher than that for the same sample annealed at 423 K. These experimental data demonstrate the increase in the GB diffusion coefficient of copper in nanostructured Ni in comparison with that happens in the coarse-grained nickel.

The interdiffusion between Ag and Au is enhanced when the Au particle size is reduced [187]. For the very small particles (<4.6 nm initial Au-core size), these two metals are almost randomly distributed within the particle; for larger particles, the diffusion boundary is only one monolayer. These results are beyond the scope

of surface pre-melting effect. Defects at the bimetallic interface seemed to enhance the radial migration of one metal into the other [187].

In situ four-point probe measurements of the onset temperature at which the electrical resistivity deviates from linearity during the temperature ramping [188] revealed that at the deviation point, the Ag thin films become unstable due to void formation and growth during annealing. In vacuum, Ag thin films thicker than 85 nm on SiO_2 substrates are thermally stable. Using the Arrhenius relation in terms of onset temperature and film thickness, an E_A of 0.326 ± 0.02 eV is obtained for the onset of Ag agglomeration ramped at a rate of 0.1 °C per second. This value is consistent with the E_A for surface diffusion of Ag in a vacuum. Therefore, Ag agglomeration and surface diffusion share the same E_A, both of which depend on the atomic cohesive energy.

The high diffusivity at the nanoscale also enhances diffusion of a liquid into the nanosolid [189]. Powder nanosolids as electrodes in chemical sensors show much improved diffusion efficiency ($10–10^4$) [189]. Further, the powder ultramicroelectrode can significantly enhance the mass transportation rate from solution to the nanosolids surface, being irrespective of particular catalytic material [190, 191].

14.4.1.2 BOLS Formulation

According to the BOLS, atomic CN imperfection suppresses the E_B that is responsible for the E_A loss in atomic diffusion, agglomeration, and glide dislocation. The diffusivity D follows the Arrhenius relation,

$$D(\infty, T) = D_0 \exp(-E_A(\infty)/k_B T) \tag{14.21}$$

where the activation enthalpy of diffusion is $E_A(\infty) = 1.76$ eV and the pre-exponential factor is $D_0 = 0.04$ cm^2 s^{-1} for gold. Incorporating the BOLS into the interdiffusion and nanoalloying by letting $E_A \propto E_B$ and hence the E_A is atomic CN dependent.

Diffusing an atom into the solid requires energy to relax partially the bonds for atom dislocations. Applying Eq. (14.12)–(14.21) by considering the size effect, one has,

$$\begin{aligned}
\frac{D(K,T)}{D(\infty,T)} &= \exp\left(-\frac{E_A(K) - E_A(\infty)}{k_B T}\right) \\
&= \exp\left(-\frac{E_A(\infty)}{k_B T}\left[\frac{E_B(K)}{E_B(\infty)} - 1\right]\right) \\
&= \exp\left(\frac{-E_A(\infty)}{k_B T}\Delta_B\right) \\
D(K,T) &= D_0 \exp\left(\frac{-E_A(\infty)}{k_B T}\frac{T_m(K)}{T_m(\infty)}\right) = D_0 \exp\left(\frac{-E_A(\infty)}{k_B T}[1 + \Delta_B]\right)
\end{aligned} \tag{14.22}$$

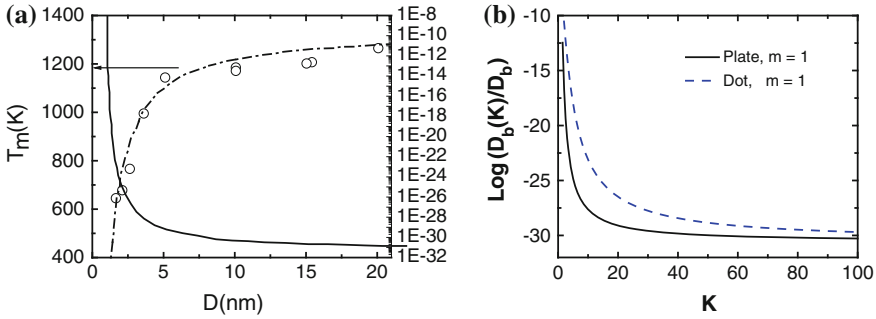

Fig. 14.9 Size dependence of the T_m and the diffusivity of silica-encapsulated gold particles. **a** The *solid curve* (*right-hand side axis*) is the calculated Au self-diffusion coefficient [78]. **b** BOLS predicted size-dependent diffusivity

Therefore, the nanodiffusivity increases at the nanoscale because of the reduced atomic E_B. The $D(K, T)$ drops with the $T_m(K)/T_m(\infty)$ ratio in an exponential way. This formulation provides a feasible mechanism for the nanoalloying, nanodiffusion, and nanoreaction in the grain boundaries where under-coordinated atoms dominate.

However, oxidation resistance of a Si nanorod exhibits oscillation features [192]. At the lower end of the size limit, Si nanorod can hardly be oxidized, as oxide tetrahedron formation is strongly subject to the atomic geometrical environment. For instance, oxidation happens preferentially at the densely packed diamond [111] plane of C_{3v} symmetry rather than the loosely packed (110) surface [193]. The high surface curvature of Si nanorod and the shortened surface bond resists the formation of an oxide tetrahedron.

Figure 14.9 compares the measured size-dependent T_m suppression and diffusion-coefficient enhancement of silica-encapsulated gold particles [78] in comparison with BOLS prediction. The trend similarity shows the correlation between the diffusivity and activity in terms of activation energy.

14.4.2 Crystal Growth

14.4.2.1 Liquid–Solid Epitaxy

Knowing the initial stages of growth of nanometer-sized crystals from the molten or amorphous matrix is a challenging issue. This process largely determines the resulting microstructure of a polycrystalline material, which is extremely difficult to study experimentally due to the small size of the clusters and the short time period involved. MD simulation results on the homoepitaxial growth and melting of Si provide an example for the understanding in terms of the transition-state theory of crystal growth.

According to transition-state theory, the driving force, F_C, for the movement of the liquid–crystal interface is the free energy difference between the liquid and bulk crystal. This difference is approximately proportional to the magnitude of the undercooling, $T_m - T$. The velocity of the moving interface, V, is proportional to the driving force $V = kF_C$, where k is the mobility of the liquid–crystal interface. This interfacial mobility determined by the movement of the atoms in the liquid phase as atoms residing in the crystalline phase are far less mobile. Therefore, this mobility is proportional to the thermally activated atomic diffusion in the liquid phase. As is well established, T_m suppression happens in a cluster of finite size due to atomic CN imperfection, which contributes to the free energy of the liquid–crystal interface.

The T_m drop with solid size is a reflection of the reduced atomic E_B and the mobility activation energy E_A ($\propto$ atomic E_B) of the liquid–crystal interface, which is essentially the same to that for liquid diffusion. In the study of growth and melting of Si, the crystal front velocity follows the Stillinger–Weber (SW) potential that consists of additive two-body and three-body energy terms. The three-body term is zero for the perfect-crystal structure at $T = 0$ K, but even at high temperature, the three-body term is relatively low in the crystalline phase (e.g., the three-body energy is about 0.1 eV/atom at T = 1,200 K). In contrast, the liquid phase is characterized by a larger three-body energy (−1 eV/atom). Using this large difference, Keblinski [86] calculated the amount of crystal and liquid phase present in the simulated cell simply by monitoring the total three-body energy and using it as reference for the corresponding values of the bulk liquid and bulk solid at the same temperature.

The size-dependent $T_m(K)$ contributes to the growth/melt behavior of clusters with various initial sizes as a function of temperature. The free energy of the cluster results from the surface and the bulk contributions. The surface contribution, U_S, approximates the product of the surface area and the liquid–solid interfacial free energy, γ_{ls}, such that $U_S = A\gamma_{ls}K^2$, where A is a geometrical constant (for a spherical dot, $A = 4\pi d_0^2$). The bulk contribution, U_B, approximates the product of the volume of the cluster and the difference in free energy densities between solid and liquid, Δu, such that $U_B = B\Delta uK^3$, where B is another geometrical constant (for a spherical cluster $B = 4\pi d_0^3/3$).

The difference between crystal and liquid free energy densities in the vicinity of the T_m is proportional to the magnitude of undercooling (or overheating), $\Delta u = u_0(T - T_m(K))$, where u_0 is a constant (Δu correctly vanishes at T_m). For a given temperature, the critical cluster size corresponds to the maximum of the free energy $U = U_S + U_B$. By differentiating the free energies with respect to the cluster size K, one finds the maximum at $T = T_m(K) - c\gamma_{sl}/K$, where c is a constant depending on A, B, and u_0. The linear dependence of the T_m on the inverse of the crystalline size implies that the interfacial energy, γ_{sl}, does not change significantly with temperature, from the first-order approximation. In reality, the interfacial energy varies with both size and temperature.

In order to understand the temperature dependence of the growth rate in terms of undercooling and thermally activated interfacial mobility, one may assume that

in the classical nucleation theory, growth takes place on an atom-by-atom basis. Hence, the average rates of crystallization and dissolution are [86]:

$$v_{\pm} = v_0 \exp\{\pm[(\Delta u - \Delta A\gamma_{sl})/(2k_B T)] - E_A/k_B T\}$$

where $\Delta A = A_{n+1} - A_n$ is an increase in the interfacial area due to the attachment of an atom to the crystal. The v is the thermal vibration frequency of the interfacial atom. The cluster growth velocity resulting from the difference between v_+ and v_-, which yields

$$\begin{aligned} V_{\text{grow}} &\sim \exp(-E_A/k_B T)\sinh\{[\Delta u - \Delta A\gamma_{sl}]/(2k_B T)\} \\ &\cong \{[\Delta u - \Delta A\gamma_{sl}]/(2k_B T)\}\exp(-E_A/k_B T) \end{aligned} \tag{14.23}$$

The argument of the hyperbolic sine is small near the T_m (it is exactly zero at the $T_m(K)$). Equation (14.23) indicates that the rate of the growth/melting is driven by the lowering of the free energy, $\Delta u - \Delta A\gamma_{sl}$, while the interfacial mobility is determined by the E_A for diffusion jumps of the interfacial atoms. Noting that ΔA is proportional to K^{-1} and $\Delta u = u_0(T - T_m(K))$, and then, the scaling law for melting applies $\Delta T_m(K) \sim \gamma_{sl}/K$. ($T_m(K)$ is the temperature at which $V_{\text{grow}} = 0$.) For planar growth, the interfacial contribution to the free energy disappears; thus, V_{grow} is zero exactly at the $T_m(\infty)$ ($\Delta u = 0$).

For a given cluster size, the free energy term can be expanded around its $T_m(K)$ such that

$$V_{\text{grow}}(K) \sim [(T_m(K) - T)/T]\exp(-E_A/k_B T) \tag{14.24}$$

This process describes the kinetics of liquid-nanosolid dissolution and growth. The E_A obtained from the best fits are 0.75 ± 0.05 eV for 2.0- and 2.6-nm solids and 0.85 ± 0.05 eV for 3.5-nm solids, respectively. This result complies with the BOLS expectation that the mean atomic E_B increases with solid size. Incorporating the BOLS correlation to the $T_m(K)$ and E_A (K), Eq. (14.24) becomes,

$$\begin{aligned} &\frac{\Delta E_A(K)}{E_A(\infty)} = \frac{\Delta T_m(K)}{T_m(\infty)} = \Delta_B \\ &V_{\text{grow}}(D) \sim [(T_m(\infty)(1+\Delta_B) - T)/T]\exp\{-[E_A(\infty)(1+\Delta_B)]/k_B T\} \end{aligned} \tag{14.25}$$

The exponential part is the same to the diffusivity (see Eq. (14.22)). Size-induced perturbation appears twice in this formulation. Results in Fig. 14.9a show the mobility of the liquid–solid interface that is determined by diffusion in the adjacent bulk liquid, which is exactly the case of homoepitaxial growth.

14.4.2.2 Vapor Phase Deposition

The knowledge of size-dependent melting provides guidelines for controlling the size of nanosolid growth on heated substrates in vapor deposition and modulating the crystal size by annealing. For a given substrate temperature (T_S), there will be a

minimum critical size of the grown particle. Thus, any particle larger than this critical size will grow and remain. If the incident sourcing cluster size is smaller than the critical size, the particles will melt upon deposition and they will coagulate to produce clusters equal to the critical size or larger. If the T_S is higher than the T_m, the landed clusters merge and then evaporate [79]. This intuition implies that the T_S should be as low as possible if one wants to obtain smaller particles.

This mechanism also applies to controlling the sinterability of nanosolids. In fact, the solid size of an oxide increases with annealing temperature [195] and agglomeration happens at a certain size range at room temperature in the process of ball milling [196, 197]. The T_S-related nucleation and agglomeration explains why the topmost Bi layers on graphite start to lose long-range order at 10–15 K below the $T_m(\infty)$ of Bi, 544.52 K and why nucleation occurs at $\sim$125 K below the $T_m(\infty)$. The temperature of melting and solidification of the same surface is different [198].

Normally, the T_S(K) for growth is around 0.3 times the $T_m(K)$ [194, 199],

$$T_S(\tau, K_C) = 0.3T_m(\tau, K) = 0.3T_m(\infty)(1 + \Delta_B)$$

$$Delta = triangle_B \cong \Delta'_B/K_C\,,$$

which gives the thermally stable critical size at the given T_S:

$$K_C = \frac{-\Delta'_B}{1 - T_S(\tau, K)/[0.3T_m(\infty)]} = \frac{\tau \sum_3 C_i\left(1 - z_{ib}C_i^{-m}\right)}{1 - T_S(\tau, K)/[0.3T_m(\infty)]} \tag{14.26}$$

The constant $\Delta'_B = -2.96$ for a spherical metallic dot ($m = 1$; $\tau = 3$; $K_C > 3$). The critical size and the number of atoms in the deposited nanosolid depend on the $T_S(\tau, K)/0.3T_m(\infty)$ ratio.

Figure 14.10b formulates the R_C (= $K_C d$) dependence on the T_S. With the known atomic size d and $T_m(\infty)$, one is able to control the crystal size [200]. This relation predicts that a monatomic layer of metals ($\tau = 1$) could only growth at $T_S = 0$ K or nearby. This prediction is in accordance with observations, For instance, monolayer Pd forms on Si surface only at 4 K or below [148].

14.4.3 Thermally Control of Crystal Size and Bandgap

Grain size that determines the bandgap of a nanosolid semiconductor is controllable by programming the growing or annealing temperature T_S [195]. For the post-annealing process, the as-grown particle size (K_0) and threshold temperature (T_{th}) are involved. The high-energy grain boundary does not gain mobility until reaching T_{th}, at which grains grow upon heating to minimize the overall energy.

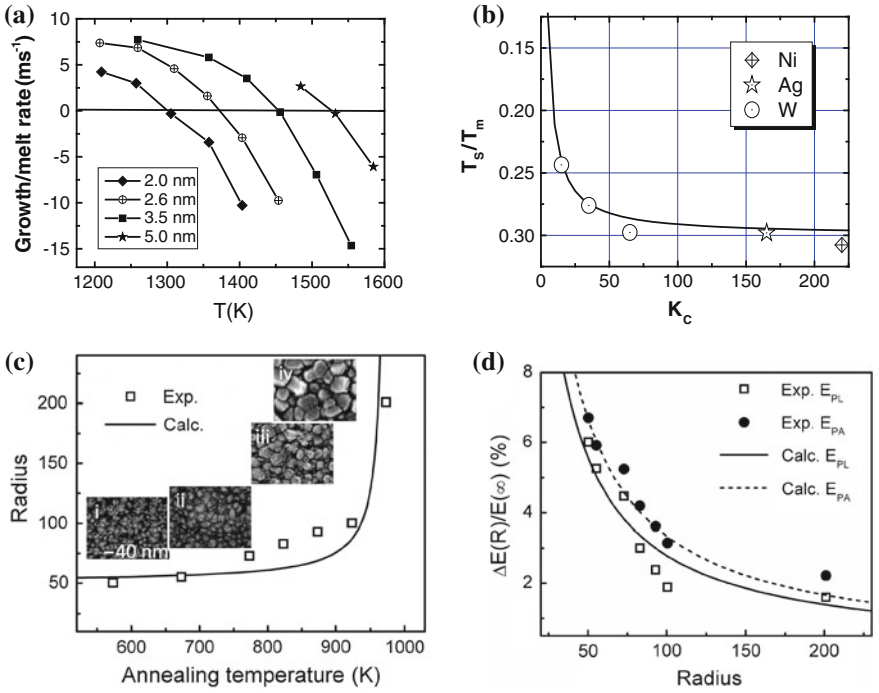

Fig. 14.10 **a** MD simulation of size and temperature dependence of Si nanosolid melting (negative) and growth (positive) [86]. **b** Agreement between BOLS predictions with measurements [194] of $T_S = 0.3T_m$ dependence of critical sizes for W ($T_m(\infty) = 3{,}695$ K), Ni (1,728 K), and Ag (1,235 K) nanocrystal growth. ZnO Size control of **c** the crystal size and **d** the E_{PL} and E_{PA} by a programmable annealing at: (1) as-grown, (2) 773 K, (3) 873 K, and (4) 923 K (Reprinted with permission from [7])

With T_{th} and K_0 being taken into consideration, Eq. (14.26) evolves into the form describing the T_a dependent of the critical size:

$$\begin{cases} T_a - T_{th} = 0.3T_m(K) = 0.3T_m(\infty)\left(1 + K^{-1}\Delta'_B\right) \\ K - K_0 = \frac{\Delta'_B}{(T_a - T_{th})/[0.3T_m(\infty)] - 1} = \frac{|\Delta'_B|}{1-(T_a - T_{th})/[0.3T_m(\infty)]} \end{cases}.$$

This relation indicates that the crystal size is dominated by the term $(T_a - T_{th})/[0.3T_m(\infty)]$; grain grows as T_a rises when $T_a > T_{th}$. The grain radius K is hence controllable by tuning the T_a.

The inset in Fig. 14.10 shows the SEM micrograph of spontaneous grain growth at different temperatures. Both the crystal size and the bandgap agree with the BOLS expectation on the T_a dependence of the physical properties.

14.5 Summary

The BOLS correlation has enabled the thermodynamic behavior of a nanosolid to be consistently formulated and understood in terms of atomic cohesive energy modulation. The difference between the cohesive energy of an atom at the surface and that of an atom inside the solid determines the fall or rise of the T_m of a surface and a nanosolid. The T_C suppression for ferromagnetic, ferroelectric, and superconducting nanosolids follows the same trend of T_m whose change follows the BOLS prediction including the short- and the long-range interactions.

Numerical match between predictions and measurements for a number of specimens reveals that the short spin–spin correlation dominates the exchange interaction in the ferromagnetic Fe, Co, Ni, and Fe_3O_2 nanosolids, whereas the long-range interaction dominates the exchange energy for the ferroelectric $PbTiO_3$, $PbZrO_3$, $SrBi_2Ta_2O_9$, and $BaTiO_3$, and the superconductive MgB_2 nanosolids.

The BOLS premise also reconciles the activation energy for diffusion, agglomeration, and nucleation in crystal growth and the temperature dependence of the crystal size in annealing and vapor–solid epitaxial growth. It is possible to tune the crystal size and properties such as the band gap of noncrystallite by controlling the processing temperatures.

References

1. W.H. Qi, M.P. Wang, Size effect on the cohesive energy of nanoparticle. J. Mater. Sci. Lett. **21**(22), 1743–1745 (2002)
2. D. Xie, M.P. Wang, W.H. Qi, A simplified model to calculate the surface-to-volume atomic ratio dependent cohesive energy of nanocrystals. J. Phy.-Condens. Matter **16**(36), L401–L405 (2004)
3. W.H. Qi, M.P. Wang, G.Y. Xu, The particle size dependence of cohesive energy of metallic nanoparticles. Chem. Phys. Lett. **372**(5–6), 632–634 (2003)
4. D. Tomanek, S. Mukherjee, K.H. Bennemann, Simple theory for the electronic and atomic-structure of small clusters. Phys. Rev. B **28**(2), 665–673 (1983)
5. Q. Jiang, J.C. Li, B.Q. Chi, Size-dependent cohesive energy of nanocrystals. Chem. Phys. Lett. **366**(5–6), 551–554 (2002)
6. H.K. Kim, S.H. Huh, J.W. Park, J.W. Jeong, G.H. Lee, The cluster size dependence of thermal stabilities of both molybdenum and tungsten nanoclusters. Chem. Phys. Lett. **354**(1–2), 165–172 (2002)
7. C.Q. Sun, Size dependence of nanostructures: Impact of bond order deficiency. Prog. Solid State Chem. **35**(1), 1–159 (2007)
8. T. Gorecki, Vacancies and changes of physical-properties of metals at melting-point. Z. Metallk. **65**(6), 426–431 (1974)
9. M.W. Finnis, The Harris functional applied to surface and vacancy formation energies in aluminum. J. Phys.-Condens. Matter **2**(2), 331–342 (1990)
10. H. Brooks, *Impurities and Imperfection* (American Socienty for Metals, Cleveland, 1955)
11. W.H. Qi, M.P. Wang, Size dependence of vacancy formation energy of metallic nanoparticles. Phys. B-Condens. Matter **334**(3–4), 432–435 (2003)
12. E.A. Brands, *Smithells Metals Reference Book*, 6th edn. (Butterworths, London, 1983)

13. A.R. Miedema, Surface energies of solid metals. Z. Metallk. **69**(5), 287–292 (1978)
14. A.N. Goldstein, C.M. Echer, A.P. Alivisatos, Melting in semiconductor nanocrystals. Science **256**(5062), 1425–1427 (1992)
15. J.G. Dash, History of the search for continuous melting. Rev. Mod. Phys. **71**(5), 1737–1743 (1999)
16. J. Penfold, The structure of the surface of pure liquids. Rep. Prog. Phys. **64**(7), 777–814 (2001)
17. V.P. Modak, H. Pathak, M. Thayer, S.J. Singer, B.E. Wyslouzil, Experimental evidence for surface freezing in supercooled n-alkane nanodroplets. Phys. Chem. Chem. Phys. **15**(18), 6783–6795 (2013)
18. J.I. Akhter, Size-dependent superheating in confined Pb(111) films. J. Phys.-Condens. Matter **17**(1), 53–60 (2005)
19. H.W. Sheng, G. Ren, L.M. Peng, Z.Q. Hu, K. Lu, Superheating and melting-point depression of Pb nanoparticles embedded in Al matrices. Philos. Mag. Lett. **73**(4), 179–186 (1996)
20. H.W. Sheng, G. Ren, L.M. Peng, Z.Q. Hu, K. Lu, Epitaxial dependence of the melting behavior of In nanoparticles embedded in Al matrices. J. Mater. Res. **12**(1), 119–123 (1997)
21. Y. Lereah, G. Deutscher, P. Cheyssac, R. Kofman, A direct observation of low-dimensional effects on melting of small lead particles. Europhys. Lett. **12**(8), 709–713 (1990)
22. A.A. Rouse, J.B. Bernhard, E.D. Sosa, D.E. Golden, Variation of field emission and photoelectric thresholds of diamond films with average grain size. Appl. Phys. Lett. **75**(21), 3417–3419 (1999)
23. N. Hamada, S. Sawada, A. Oshiyama, New one-dimensional conductors—graphitic microtubules. Phys. Rev. Lett. **68**(10), 1579–1581 (1992)
24. V.P. Skripov, V.P. Koverda, V.N. Skokov, Size effect on melting of small particle. Phys. Status Solidi A-Appl. Res. **66**(1), 109–118 (1981)
25. J.F. Pocza, A. Barna, P.B. Barna, Formation processes of vacuum-deposited indium films and thermodynamical properties of submicroscopic particles observed by in situ electron microscopy. J. Vacuum Sci. Technol. **6**(4), 472–474 (1969)
26. Y.J. Lee, E.K. Lee, S. Kim, R.M. Nieminen, Effect of potential energy distribution on the melting of clusters. Phys. Rev. Lett. **86**(6), 999–1002 (2001)
27. S.C. Santucci, A. Goldoni, R. Larciprete, S. Lizzit, M. Bertolo, A. Baraldi, C. Masciovecchio, Calorimetry at surfaces using high-resolution core-level photoemission. Phys. Rev. Lett. **93**(10), 106105 (2004)
28. P. Bergese, I. Colombo, D. Gervasoni, L.E. Depero, Melting of nanostructured drugs embedded into a polymeric matrix. J. Phys. Chem. B **108**(40), 15488–15493 (2004)
29. I.S. Hwang, S.H. Chang, C.K. Fang, L.J. Chen, T.T. Tsong, Observation of finite-size effects on a structural phase transition of 2D nanoislands. Phys. Rev. Lett. **93**(10), 106101 (2004)
30. L. Miao, V.R. Bhethanabotla, B. Joseph, Melting of Pd clusters and nanowires: A comparison study using molecular dynamics simulation. Phys. Rev. B **72**(13), 134109 (2005)
31. F.G. Shi, Size-dependent thermal vibrations and melting in nanocrystals. J. Mater. Res. **9**(5), 1307–1313 (1994)
32. P. Buffat, J.P. Borel, Size effect on melting temperature of gold particles. Phys. Rev. A **13**(6), 2287–2298 (1976)
33. P. Pawlow, The dependency of the melting point on the surface energy of a solid body (Supplement). Zeitschrift Fur Physikalische Chemie–Stochiometrie Und Verwandtschaftslehre **65**(5), 545–548 (1909)
34. H. Reiss, P. Mirabel, R.L. Whetten, Capillarity theory for the coexistence of liquid and solid clusters. J. Phys. Chem. **92**(26), 7241–7246 (1988)
35. H. Sakai, Surface-induced melting of small particles. Surf. Sci. **351**(1–3), 285–291 (1996)
36. K.J. Hanszen, Theoretische untersuchungen uber den schmelzpunkt kleiner kugelchen—ein beitrag zur thermodynamik der grenzflachen. Z. Angew. Phys. **157**(5), 523–553 (1960)

37. P.R. Couchman, W.A. Jesser, Thermodynamic theory of size dependence of melting temperature in metals. Nature **269**(5628), 481–483 (1977)
38. R.R. Vanfleet, J.M. Mochel, Thermodynamics of melting and freezing in small particles. Surf. Sci. **341**(1–2), 40–50 (1995)
39. B. Vekhter, R.S. Berry, Phase coexistence in clusters: an ''experimental'' isobar and an elementary model. J. Chem. Phys. **106**(15), 6456–6459 (1997)
40. Q. Jiang, Z. Zhang, J.C. Li, Superheating of nanocrystals embedded in matrix. Chem. Phys. Lett. **322**(6), 549–552 (2000)
41. M. Zhang, M.Y. Efremov, F. Schiettekatte, E.A. Olson, A.T. Kwan, S.L. Lai, T. Wisleder, J.E. Greene, L.H. Allen, Size-dependent melting point depression of nanostructures: nanocalorimetric measurements. Phys. Rev. B **62**(15), 10548–10557 (2000)
42. Z.H. Jin, P. Gumbsch, K. Lu, E. Ma, Melting mechanisms at the limit of superheating. Phys. Rev. Lett. **87**(5), 055703 (2001)
43. R. Defay, I. Prigogine, *Surface Tension and Adsorption* (Wiley, New York, 1951)
44. K.F. Peters, J.B. Cohen, Y.W. Chung, Melting of Pb nanocrystals. Phys. Rev. B **57**(21), 13430–13438 (1998)
45. U. Tartaglino, T. Zykova-Timan, F. Ercolessi, E. Tosatti, Melting and nonmelting of solid surfaces and nanosystems. Phys. Rep.-Rev. Sec. Phys. Lett. **411**(5), 291–321 (2005)
46. Q.W. Yang, R.Z. Zhu, J.A. Wei, Y.H. Wen, Surface-induced melting of metal nanoclusters. Chin. Phys. Lett. **21**(11), 2171–2174 (2004)
47. K.K. Nanda, S.N. Sahu, S.N. Behera, Liquid-drop model for the size-dependent melting of low-dimensional systems. Phys. Rev. A **66**(1), 013208 (2002)
48. J.H. Rose, J.R. Smith, J. Ferrante, Universal features of bonding in metals. Phys. Rev. B **28**(4), 1835–1845 (1983)
49. J. Tateno, Empirical relation on melting temperature of some ionic-crystals. Solid State Commun. **10**(1), 61–62 (1972)
50. M.A. Omar, *Elementary Solid State Physics: Principles and Applications* (Addison-Wesley, New York, 1993)
51. B. Pluis, D. Frenkel, J.F. Vanderveen, Surface-induced melting and freezing II. A semi-empirical landau-type model. Surf. Sci. **239**(3), 282–300 (1990)
52. M. Wautelet, Estimation of the variation of the melting temperature with the size of small particles, on the basis of a surface-phonon instability model. J. Phys. D-Appl. Phys. **24**(3), 343–346 (1991)
53. R. Vallee, M. Wautelet, J.P. Dauchot, M. Hecq, Size and segregation effects on the phase diagrams of nanoparticles of binary systems. Nanotechnology **12**(1), 68–74 (2001)
54. M. Wautelet, Phase stability of electronically excited Si nanoparticles. J. Phys.-Condens. Matter **16**(12), L163–L166 (2004)
55. Q. Jiang, L.H. Liang, J.C. Li, Thermodynamic superheating and relevant interface stability of low-dimensional metallic crystals. J. Phys.: Condens. Matter **13**(4), 565–571 (2001)
56. Q. Jiang, H.Y. Tong, D.T. Hsu, K. Okuyama, F.G. Shi, Thermal stability of crystalline thin films. Thin Solid Films **312**(1–2), 357–361 (1998)
57. Q. Jiang, H.X. Shi, J.C. Li, Finite size effect on glass transition temperatures. Thin Solid Films **354**(1–2), 283–286 (1999)
58. Z. Wen, M. Zhao, Q. Jiang, The melting temperature of molecular nanocrystals at the lower bound of the mesoscopic size range. J. Phys.-Condens. Matter **12**(41), 8819–8824 (2000)
59. Q. Jiang, L.H. Liang, M. Zhao, Modelling of the melting temperature of nano-ice in MCM-41 pores. J. Phys.-Condens. Matter **13**(20), L397–L401 (2001)
60. F.A. Lindemann, The calculation of molecular natural frequencies. Physikalische Zeitschrift **11**, 609–612 (1910)
61. Z. Zhang, J.C. Li, Q. Jiang, Modelling for size-dependent and dimension-dependent melting of nanocrystals. J. Phys. D-Appl. Phys. **33**(20), 2653–2656 (2000)
62. J.L. Wang, X.S. Chen, G.H. Wang, B.L. Wang, W. Lu, J.J. Zhao, Melting behavior in ultrathin metallic nanowires. Phys. Rev. B **66**(8), 085408 (2002)

63. W.Y. Hu, S.G. Xiao, J.Y. Yang, Z. Zhang, Melting evolution and diffusion behavior of vanadium nanoparticles. Eur. Phys. J. B **45**(4), 547–554 (2005)
64. S.L. Lai, J.Y. Guo, V. Petrova, G. Ramanath, L.H. Allen, Size-dependent melting properties of small tin particles: Nanocalorimetric measurements. Phys. Rev. Lett. **77**(1), 99–102 (1996)
65. Q. Jiang, X.Y. Lang, Glass transition of low-dimensional polystyrene. Macromol. Rapid Commun. **25**(7), 825–828 (2004)
66. X.Z. Ding, X.H. Liu, The Debye temperature of nanocrystalline titania measured by two different methods. Phys. Status Solidi A-Appl. Res. **158**(2), 433–439 (1996)
67. M. Schmidt, R. Kusche, B. von Issendorff, H. Haberland, Irregular variations in the melting point of size-selected atomic clusters. Nature **393**(6682), 238–240 (1998)
68. S.L. Lai, J.R.A. Carlsson, L.H. Allen, Melting point depression of Al clusters generated during the early stages of film growth: nanocalorimetry measurements. Appl. Phys. Lett. **72**(9), 1098–1100 (1998)
69. C.E. Bottani, A.L. Bassi, B.K. Tanner, A. Stella, P. Tognini, P. Cheyssac, R. Kofman, Melting in metallic Sn nanoparticles studied by surface Brillouin scattering and synchrotron-x-ray diffraction. Phys. Rev. B **59**(24), 15601–15604 (1999)
70. J. Zhong, L.H. Zhang, Z.H. Jin, M.L. Sui, K. Lu, Superheating of Ag nanoparticles embedded in Ni matrix. Acta Mater. **49**(15), 2897–2904 (2001)
71. O.G. Shpyrko, A.Y. Grigoriev, C. Steimer, P.S. Pershan, B.H. Lin, M. Meron, T. Graber, J. Gerbhardt, B. Ocko, M. Deutsch, Anomalous layering at the liquid Sn surface. Phys. Rev. B **70**(22), 224206 (2004)
72. L. Lu, R. Schwaiger, Z.W. Shan, M. Dao, K. Lu, S. Suresh, Nano-sized twins induce high rate sensitivity of flow stress in pure copper. Acta Mater. **53**(7), 2169–2179 (2005)
73. S. Veprek, M.G.J. Veprek-Heijman, P. Karvankova, J. Prochazka, Different approaches to superhard coatings and nanocomposites. Thin Solid Films **476**(1), 1–29 (2005)
74. S.G. Srinivasan, X.Z. Liao, M.I. Baskes, R.J. McCabe, Y.H. Zhao, Y.T. Zhu, Compact and dissociated dislocations in aluminum: Implications for deformation. Phys. Rev. Lett. **94**(12), 125502 (2005)
75. F. Ding, A. Rosen, K. Bolton, Size dependence of the coalescence and melting of iron clusters: a molecular-dynamics study. Phys. Rev. B **70**(7), 075416 (2004)
76. C.Q. Sun, Y. Shi, C.M. Li, S. Li, T.C.A. Yeung, Size-induced undercooling and overheating in phase transitions in bare and embedded clusters. Phys. Rev. B **73**(7), 075408 (2006)
77. M.J. Sinnott, *The solid state for engineers* (Wiley, New York, 1963)
78. K. Dick, T. Dhanasekaran, Z.Y. Zhang, D. Meisel, Size-dependent melting of silica-encapsulated gold nanoparticles. J. Am. Chem. Soc. **124**(10), 2312–2317 (2002)
79. K.K. Nanda, A. Maisels, F.E. Kruis, H. Fissan, S. Stappert, Higher surface energy of free nanoparticles. Phys. Rev. Lett. **91**(10), 106102 (2003)
80. J. Eckert, J.C. Holzer, C.C. Ahn, Z. Fu, W.L. Johnson, Melting behavior of nanocrystalline aluminum powders. Nanostruc Mater **2**(4), 407–413 (1993)
81. S.L. Lai, G. Ramanath, L.H. Allen, P. Infante, Heat capacity measurements of Sn nanostructures using a thin-film differential scanning calorimeter with 0.2 nJ sensitivity. Appl. Phys. Lett. **70**(1), 43–45 (1997)
82. G.L. Allen, W.W. Gile, W.A. Jesser, The melting temperature of micro-crystals embedded in a matrix. Acta Metall. **28**(12), 1695–1701 (1980)
83. K.M. Unruh, T.E. Huber, C.A. Huber, Melting and freezing behavior of indium metal in porous glasses. Phys. Rev. B **48**(12), 9021–9027 (1993)
84. T. Bendavid, Y. Lereah, G. Deutscher, R. Kofman, P. Cheyssac, Solid-liquid transition in ultra-fine lead particles. Philos. Mag. A:-Phys. Condens. Matter Struct. Defects Mech. Prop. **71**(5), 1135–1143 (1995)
85. A.N. Goldstein, The melting of silicon nanocrystals: Submicron thin-film structures derived from nanocrystal precursors. Appl. Phys. A-Mater. Sci. Process. **62**(1), 33–37 (1996)

86. P. Keblinski (1999) Thermodynamics and kinetics of melting and growth of crystalline silicon clusters, in *Microcrystalline and Nanocrystalline Semiconductors-1998*, ed. by L.T. Canham et al., pp 311–316
87. Y.Y. Wu, P.D. Yang, Melting and welding semiconductor nanowires in nanotubes. Adv. Mater. **13**(7), 520–523 (2001)
88. G. Kellermann, A.F. Craievich, Structure and melting of Bi nanocrystals embedded in a B_2O_3-Na_2O glass. Physical Review B **65**(13), 134204 (2002)
89. S.J. Peppiatt, Melting of small particles II. Bismuth. Proc. R. Soc. London Ser. A-Math. Phys. Eng. Sci. **345**(1642), 401–412 (1975)
90. H. Itoigawa, T. Kamiyama, Y. Nakamura, Bi precipitates in Na_2O–B_2O_3 glasses. J. Non-Cryst. Solids **210**(1), 95–100 (1997)
91. K. Morishige, K. Kawano, Freezing and melting of nitrogen, carbon monoxide, and krypton in a single cylindrical pore. J. Phys. Chem. B **104**(13), 2894–2900 (2000)
92. E. Molz, A.P.Y. Wong, M.H.W. Chan, J.R. Beamish, Freezing and melting of fluids in porous glass. Phys. Rev. B **48**(9), 5741–5750 (1993)
93. H. Saka, Y. Nishikawa, T. Imura, Temperature dependence of the stacking fault energy in silver-base alloys. Phil. Mag. A **57**, 859–868 (1983)
94. L. Grabaek, J. Bohr, E. Johnson, A. Johansen, L. Sarholtkristensen, H.H. Andersen, Superheating and supercooling of lead precipitates in aluminum. Phys. Rev. Lett. **64**(8), 934–937 (1990)
95. L. Zhang, Z.H. Jin, L.H. Zhang, M.L. Sui, K. Lu, Superheating of confined Pb thin films. Phys. Rev. Lett. **85**(7), 1484–1487 (2000)
96. K. Chattopadhyay, R. Goswami, Melting and superheating of metals and alloys. Prog. Mater Sci. **42**(1–4), 287–300 (1997)
97. G.A. Breaux, R.C. Benirschke, T. Sugai, B.S. Kinnear, M.F. Jarrold, Hot and solid gallium clusters: too small to melt. Phys. Rev. Lett. **91**(21), 215508 (2003)
98. S. Chacko, K. Joshi, D.G. Kanhere, S.A. Blundell, Why do gallium clusters have a higher melting point than the bulk? Phys. Rev. Lett. **92**(13), 135506 (2004)
99. Z.Y. Lu, C.Z. Wang, K.M. Ho, Structures and dynamical properties of C-n, Si-n, Ge-n, and Sn-n clusters with n up to 13. Phys. Rev. B **61**(3), 2329–2334 (2000)
100. F.C. Chuang, C.Z. Wang, S. Ogut, J.R. Chelikowsky, K.M. Ho, Melting of small Sn clusters by ab initio molecular dynamics simulations. Phys. Rev. B **69**(16), 165408 (2004)
101. K. Joshi, D.G. Kanhere, S.A. Blundell, Abnormally high melting temperature of the Sn-10 cluster. Phys. Rev. B **66**(15), 155329 (2002)
102. G.A. Breaux, C.M. Neal, B.P. Cao, M.F. Jarrold, Tin clusters that do not melt: Calorimetry measurements up to 650 K. Phys. Rev. B **71**(7), 073410 (2005)
103. E.A. Olson, M.Y. Efremov, M. Zhang, Z. Zhang, L.H. Allen, Size-dependent melting of Bi nanoparticles. J. Appl. Phys. **97**(3), 034304 (2005)
104. R.O. Jones, Simulated annealing study of neutral and charged clusters—Al(n) and Ga(n). J. Chem. Phys. **99**(2), 1194–1206 (1993)
105. A.A. Shvartsburg, B. Liu, Z.Y. Lu, C.Z. Wang, M.F. Jarrold, K.M. Ho, Structures of germanium clusters: Where the growth patterns of silicon and germanium clusters diverge. Phys. Rev. Lett. **83**(11), 2167–2170 (1999)
106. G.H. Lu, S.H. Deng, T.M. Wang, M. Kohyama, R. Yamamoto, Theoretical tensile strength of an Al grain boundary. Phys. Rev. B **69**(13), 134106 (2004)
107. K. Carling, G. Wahnstrom, T.R. Mattsson, A.E. Mattsson, N. Sandberg, G. Grimvall, Vacancies in metals: from first-principles calculations to experimental data. Phys. Rev. Lett. **85**(18), 3862–3865 (2000)
108. S. Ogata, J. Li, S. Yip, Ideal pure shear strength of aluminum and copper. Science **298**(5594), 807–811 (2002)
109. G.A. Breaux, C.M. Neal, B. Cao, M.F. Jarrold, Melting, premelting, and structural transitions in size-selected aluminum clusters with around 55 atoms. Phys. Rev. Lett. **94**(17), 173401 (2005)

110. H.H. Liu, E.Y. Jiang, H.L. Bai, P. Wu, Z.Q. Li, C.Q. Sun, Possible paths towards magic clusters formation. THEOCHEM **728**(1–3), 203–207 (2005)
111. H. Haberland, T. Hippler, J. Donges, O. Kostko, M. Schmidt, B. von Issendorff, Melting of sodium clusters: where do the magic numbers come from? Phys. Rev. Lett. **94**(3), 035701 (2005)
112. T. Bachels, H.J. Guntherodt, R. Schafer, Melting of isolated tin nanoparticles. Phys. Rev. Lett. **85**(6), 1250–1253 (2000)
113. C.Q. Sun, C.M. Li, H.L. Bai, E.Y. Jiang, Melting point oscillation of a solid over the whole range of sizes. Nanotechnology **16**(8), 1290–1293 (2005)
114. F. Huang, G.J. Mankey, M.T. Kief, R.F. Willis, Finite-size-scaling behavior of ferromagnetic thin-films. J. Appl. Phys. **73**(10), 6760–6762 (1993)
115. G.G. Kenning, J.M. Slaughter, J.A. Cowen, Finite-size effects in a CuMn spin-glass. Phys. Rev. Lett. **59**(22), 2596–2599 (1987)
116. Z.Q. Qiu, J. Pearson, S.D. Bader, Asymmetry of the spin reorientation transition in ultrathin fe films and wedges grown on Ag(100). Phys. Rev. Lett. **70**(7), 1006–1009 (1993)
117. W.L. Zhong, B. Jiang, P.L. Zhang, J.M. Ma, H.M. Cheng, Z.H. Yang, L.X. Li, Phase-transition in $PbTiO_3$ ultrafine particles of different sizes. J. Phys.: Condens. Matter **5**(16), 2619–2624 (1993)
118. K. Ishikawa, K. Yoshikawa, N. Okada, Size effect on the ferroelectric phase-transition in $PbTiO_3$ ultrafine particles. Phys. Rev. B **37**(10), 5852–5855 (1988)
119. T. Yu, Z.X. Shen, W.S. Toh, J.M. Xue, J. Wang, Size effect on the ferroelectric phase transition in $SrBi_2Ta_2O_9$ nanoparticles. J. Appl. Phys. **94**(1), 618–620 (2003)
120. A.V. Pogrebnyakov, J.M. Redwing, J.E. Jones, X.X. Xi, S.Y. Xu, Q. Li, V. Vaithyanathan, D.G. Schlom, Thickness dependence of the properties of epitaxial MgB2 thin films grown by hybrid physical-chemical vapor deposition. Appl. Phys. Lett. **82**(24), 4319–4321 (2003)
121. A.P. Tsai, N. Chandrasekhar, K. Chattopadhyay, Size effect on the superconducting transition of embedded lead particles in an Al-Cu-V amorphous matrix. Appl. Phys. Lett. **75**(11), 1527–1528 (1999)
122. I. Giaever, H.R. Zeller, Superconductivity of small TiN particles measured by tunneling. Phys. Rev. Lett. **20**(26), 1504–1508 (1968)
123. M. Stampanoni, A. Vaterlaus, M. Aeschlimann, F. Meier, Magnetism of epitaxial bcc iron on Ag(001) observed by spin-polarized photoemission. Phys. Rev. Lett. **59**(21), 2483–2485 (1987)
124. M.N. Baibich, J.M. Broto, A. Fert, F.N. Vandau, F. Petroff, P. Eitenne, G. Creuzet, A. Friederich, J. Chazelas, Giant magnetoresistance of (001)Fe/(001) Cr magnetic superlattices. Phys. Rev. Lett. **61**(21), 2472–2475 (1988)
125. C. Liu, E.R. Moog, S.D. Bader, Polar Kerr-effect observation of perpendicular surface anisotropy for ultrathin fcc Fe grown on Cu(100). Phys. Rev. Lett. **60**(23), 2422–2425 (1988)
126. C.M. Schneider, P. Bressler, P. Schuster, J. Kirschner, J.J. Demiguel, R. Miranda, Curie-temperature of ultrathin films of fcc cobalt epitaxially grown on atomically flat Cu(100) surfaces. Phys. Rev. Lett. **64**(9), 1059–1062 (1990)
127. X. Hu, Y. Kawazoe, Mean-field theory for critical phenomena in bilayer systems. Phys. Rev. B **50**(17), 12647–12658 (1994)
128. J.T. Ou, F.R. Wang, D.L. Lin, Critical behavior of magnetic films in the Ising model. Phys. Rev. E **56**(3), 2805–2810 (1997)
129. Y. Li, K. Baberschke, Dimensional crossover in ultrathin Ni(111) films on W(110). Phys. Rev. Lett. **68**(8), 1208–1211 (1992)
130. M. Tischer, D. Arvanitis, T. Yokoyama, T. Lederer, L. Troger, K. Baberschke, Temperature-dependent mcxd measurements of thin Ni films on Cu(100). Surf. Sci. **307**, 1096–1101 (1994)
131. L.H. Tjeng, Y.U. Idzerda, P. Rudolf, F. Sette, C.T. Chen, Soft-x-ray magnetic circular-dichroism—a new technique for probing magnetic-properties of magnetic-surfaces and ultrathin films. J. Magn. Magn. Mater. **109**(2–3), 288–292 (1992)

132. J.S. Jiang, C.L. Chien, Magnetization and finite-size effects in Gd/W multilayers. J. Appl. Phys. **79**(8), 5615–5617 (1996)
133. J.S. Jiang, D. Davidovic, D.H. Reich, C.L. Chien, Oscillatory superconducting transition-temperature in Nb/Gd multilayers. Phys. Rev. Lett. **74**(2), 314–317 (1995)
134. P.H. Zhou, D.S. Xue, Finite-size effect on magnetic properties in Prussian blue nanowire arrays. J. Appl. Phys. **96**(1), 610–614 (2004)
135. M.E. Fisher, M.N. Barber, Scaling theory for finite-size effects in critical region. Phys. Rev. Lett. **28**(23), 1516–1519 (1972)
136. D.S. Ritchie, M.E. Fisher, Finite-size and surface effects in Heisenberg films. Phys. Rev. B **7**(1), 480–494 (1973)
137. M.N. Barber, in *Phase Transitions and Critical Phenomena*, ed. by C. Domb, J. Lebowita, Vol. 8 (Academic, New York, 1983)
138. R.J. Zhang, R.F. Willis, Thickness-dependent Curie temperatures of ultrathin magnetic films: Effect of the range of spin–spin interactions. Phys. Rev. Lett. **86**(12), 2665–2668 (2001)
139. V.I. Nikolaev, A.M. Shipilin, The influence of breaking of exchange bonds on the Curie temperature. Phys. Solid State **45**(6), 1079–1080 (2003)
140. B. Sadeh, M. Doi, T. Shimizu, M.J. Matsui, Dependence of the Curie temperature on the diameter of Fe_3O_4 ultra-fine particles. J Magn Soc Jpn **24**, 511–514 (2000)
141. P.G. Degennes, *Superconductivity of Metals and Alloys* (Benjamin, New York, 1966)
142. R. Goswami, S. Banerjee, K. Chattopadhyay, A.K. Raychaudhuri, Superconductivity in rapidly quenched metallic systems with nanoscale structure. J. Appl. Phys. **73**(6), 2934–2940 (1993)
143. C.Q. Sun, Surface and nanosolid core-level shift: Impact of atomic coordination-number imperfection. Phys. Rev. B **69**(4), 045105 (2004)
144. R. Kubo, Electronic properties of metallic fine particles. I. J. Phys. Soc. Jpn. **17**(6), 975–979 (1962)
145. P.W. Anderson, Theory of dirty superconductors. J. Phys. Chem. Solids **11**(1–2), 26–30 (1959)
146. M. Strongin, R.S. Thompson, O.F. Kammerer, J.E. Crow, Destruction of superconductivity in disordered near-monolayer films. Phys. Rev. B **1**(3), 1078–1090 (1970)
147. B. Muhlschl, Dj Scalapin, R. Denton, *Thermodynamic properties of small superconducting particles*. Phys. Rev. B **6**(5), 1767 (1972)
148. Y. Guo, Y.F. Zhang, X.Y. Bao, T.Z. Han, Z. Tang, L.X. Zhang, W.G. Zhu, E.G. Wang, Q. Niu, Z.Q. Qiu, J.F. Jia, Z.X. Zhao, Q.K. Xue, Superconductivity modulated by quantum size effects. Science **306**(5703), 1915–1917 (2004)
149. A.V. Pogrebnyakov, J.M. Redwing, S. Raghavan, V. Vaithyanathan, D.G. Schlom, S.Y. Xu, Q. Li, D.A. Tenne, A. Soukiassian, X.X. Xi, M.D. Johannes, D. Kasinathan, W.E. Pickett, J.S. Wu, J.C.H. Spence, Enhancement of the superconducting transition temperature of MgB_2 by a strain-induced bond-stretching mode softening. Phys. Rev. Lett. **93**(14), 147006 (2004)
150. J. Nagamatsu, N. Nakagawa, T. Muranaka, Y. Zenitani, J. Akimitsu, Superconductivity at 39 K in magnesium diboride. Nature **410**(6824), 63–64 (2001)
151. N. Hur, P.A. Sharma, S. Guha, M.Z. Cieplak, D.J. Werder, Y. Horibe, C.H. Chen, S.W. Cheong, High-quality MgB2 films on boron crystals with onset T-c of 41.7 K. Appl. Phys. Lett. **79**(25), 4180–4182 (2001)
152. T. Yildirim, O. Gulseren, A simple theory of 40 K superconductivity in MgB_2: first-principles calculations of T-c its dependence on boron mass and pressure. J. Phys. Chem. Solids **63**(12), 2201–2206 (2002)
153. V. Hornebecq, C. Huber, M. Maglione, M. Antonietti, C. Elissalde, Dielectric properties of pure (BaSr)TiO3 and composites with different grain sizes ranging from the nanometer to the micrometer. Adv. Funct. Mater. **14**(9), 899–904 (2004)

154. Z. Zhao, V. Buscaglia, M. Viviani, M.T. Buscaglia, L. Mitoseriu, A. Testino, M. Nygren, M. Johnsson, P. Nanni, Grain-size effects on the ferroelectric behavior of dense nanocrystalline $BaTiO_3$ ceramics. Phys. Rev. B **70**(2), 024107 (2004)
155. J. Hong, H.W. Song, J. Choi, S.K. Kim, Y. Kim, K. No, Dependence of ferroelectricity on film thickness in nano-scale Pb(Zr, Ti)O-3 thin films. Integr. Ferroelectr. **68**, 157–159 (2004)
156. W.P. Tong, N.R. Tao, Z.B. Wang, J. Lu, K. Lu, Nitriding iron at lower temperatures. Science **299**(5607), 686–688 (2003)
157. C.L. Wang, Y. Xin, X.S. Wang, W.L. Zhong, Size effects of ferroelectric particles described by the transverse Ising model. Phys. Rev. B **62**(17), 11423–11427 (2000)
158. B. Jiang, L.A. Bursill, Phenomenological theory of size effects in ultrafine ferroelectric particles of lead titanate. Phys. Rev. B **60**(14), 9978–9982 (1999)
159. H.T. Huang, C.Q. Sun, T.S. Zhang, P. Hing, Grain-size effect on ferroelectric Pb(Zr1-xTix)O-3 solid solutions induced by surface bond contraction. Phys. Rev. B **63**(18), 184112 (2001)
160. H.T. Huang, C.Q. Sun, P. Hing, Surface bond contraction and its effect on the nanometric sized lead zirconate titanate. J. Phys.: Condens. Matter **12**(6), L127–L132 (2000)
161. M. Tanaka, Y. Makino, Finite size effects in submicron barium titanate particles. Ferroelectr. Lett. Sect. **24**(1–2), 13–23 (1998)
162. A. Munkholm, S.K. Streiffer, M.V.R. Murty, J.A. Eastman, C. Thompson, O. Auciello, L. Thompson, J.F. Moore, G.B. Stephenson, Antiferrodistortive reconstruction of the PbTiO3(001) surface. Phys. Rev. Lett. **88**(1), 016101 (2002)
163. H.T. Huang, L.M. Zhou, J. Guo, H.H. Hng, J.T. Oh, P. Hing, F spots and domain patterns in rhombohedral PbZr0.90Ti0.10O3. Appl. Phys. Lett. **83**(18), 3692–3694 (2003)
164. Q. Jiang, X.F. Cui, M. Zhao, Size effects on Curie temperature of ferroelectric particles. Appl. Phys. A-Mater. Sci. Process. **78**(5), 703–704 (2004)
165. R.D. Zysler, D. Fiorani, A.M. Testa, L. Suber, E. Agostinelli, M. Godinho, Size dependence of the spin-flop transition in hematite nanoparticles. Phys. Rev. B **68**(21), 212408 (2003)
166. N. Amin, S. Arajs, Morin temperature of annealed submicronic alpha-Fe_2O_3 particles. Phys. Rev. B **35**(10), 4810–4811 (1987)
167. E. Weschke, H. Ott, E. Schierle, C. Schussler-Langeheine, D.V. Vyalikh, G. Kaindl, V. Leiner, M. Ay, T. Schmitte, H. Zabel, P.J. Jensen, Finite-size effect on magnetic ordering temperatures in long-period antiferromagnets: holmium thin films. Phys. Rev. Lett. **93**(15), 157204 (2004)
168. E.E. Fullerton, K.T. Riggs, C.H. Sowers, S.D. Bader, A. Berger, Suppression of biquadratic coupling in Fe/Cr(001) superlattices below the neel transition of Cr. Phys. Rev. Lett. **75**(2), 330–333 (1995)
169. S.S. Rao, K.N. Anuradha, S. Sarangi, S.V. Bhat, Weakening of charge order and antiferromagnetic to ferromagnetic switch over in $Pr0.5Ca0.5MnO_3$ nanowires. Appl. Phys. Lett. **87**(18), 182503 (2005)
170. S.Z. Ma, X.H. Wang, J. Zhou, L.T. Li, C.Q. Sun, Thermal stability of the nanostructured BaTiO3 determined by long and short range interactions: a dual-shell model. J. Appl. Phys. **107**(6), 064102 (2010)
171. W.H. Zhong, C.Q. Sun, B.K. Tay, S. Li, H.L. Bai, E.Y. Jiang, Curie temperature suppression of ferromagnetic nanosolids. J. Phys.: Condens. Matter **14**(23), L399–L405 (2002)
172. R. Bergholz, U. Gradmann, Structure and magnetism of oligatomic Ni(111)-films on Re(0001). J. Magn. Magn. Mater. **45**(2–3), 389–398 (1984)
173. K. Uchina, Y. Sadanaga, T. Hirose, J Am Ceram Soc. **72**, 1555 (1999)
174. S. Chattopadhyay, P. Ayyub, V.R. Palkar, A.V. Gurjar, R.M. Wankar, M. Multani, Finite-size effects in antiferroelectric $PbZrO_3$ nanoparticles. J. Phys.-Condens Matter **9**(38), 8135–8145 (1997)
175. S. Li, T. White, J. Plevert, C.Q. Sun, Superconductivity of nano-crystalline MgB_2. Supercond. Sci. Technol. **17**(9), S589–S594 (2004)

176. S. Li, T. White, C.Q. Sun, Y.Q. Fu, J. Plevert, K. Lauren, Discriminating lattice structural effects from electronic contributions to the superconductivity of doped MgB_2 with nanotechnology. J. Phys. Chem. B **108**(42), 16415–16419 (2004)
177. S. Schlag, H.F. Eicke, W.B. Stern, Size driven phase transition and thermodynamic properties of nanocrystalline $BaTiO_3$. Ferroelectr. Lett. Sect. **173**, 351–369 (1995)
178. R.Z. Valiev, R.K. Islamgaliev, I.V. Alexandrov, Bulk nanostructured materials from severe plastic deformation. Prog. Mater Sci. **45**(2), 103–189 (2000)
179. G. Ouyang, C.X. Wang, G.W. Yang, Anomalous interfacial diffusion in immiscible metallic multilayers: a size-dependent kinetic approach. Appl. Phys. Lett. **86**(17), 171914 (2005)
180. I.M. Razumovskii, L.G. Kornelyuk, R.Z. Valiev, V.I. Sergeev, Diffusion along nonequilibrium grain-boundaries in a nickel-base superalloy. Mater. Sci. Eng., A:-Struct. Mater. Prop. Microstruct and Processing **167**(1–2), 123–127 (1993)
181. J. Horvath, Diffusion in nanocrystalline materials diffusion and defect data—Solid State Data. Part A: Defect Diffus. Forum **66–69**, 207–227 (1989)
182. T. Mutschele, R. Kirchheim, Segregation and diffusion of hydrogen in grain-boundaries of palladium. Scr. Metall. **21**(2), 135–140 (1987)
183. Y.R. Kolobov, G.P. Grabovetskaya, I.V. Ratochka, E.V. Kabanova, E.V. Naidenkin, T.C. Lowe, Effect of grain-boundary diffusion fluxes of copper on the acceleration of creep in submicrocrystalline nickel. Ann. Chim.-Sci. Mat. **21**(6-7), 483–491 (1996)
184. R. Wurschum, A. Kubler, S. Gruss, P. Acharwaechter, W. Frank, R.Z. Valiev, R.R. Mulyukov, H.E. Schaeffer, Tracer diffusion and crystallite growth in ultra-fine-grained Pd prepared by severe plastic deformation. Ann. Chim.-Sci. Mat. **21**(6-7), 471–482 (1996)
185. Z.B. Wang, N.R. Tao, W.P. Tong, J. Lu, K. Lu, Diffusion of chromium in nanocrystalline iron produced by means of surface mechanical attrition treatment. Acta Mater. **51**(14), 4319–4329 (2003)
186. Y.M. Mishin, I.M. Razumovskii, Development of boundary diffusion-models. Scr. Metall. Materialia **25**(6), 1375–1380 (1991)
187. T. Shibata, B.A. Bunker, Z.Y. Zhang, D. Meisel, C.F. Vardeman, J.D. Gezelter, Size-dependent spontaneous alloying of Au-Ag nanoparticles. J. Am. Chem. Soc. **124**(40), 11989–11996 (2002)
188. H.C. Kim, T.L. Alford, D.R. Allee, Thickness dependence on the thermal stability of silver thin films. Appl. Phys. Lett. **81**(22), 4287–4289 (2002)
189. C.M. Li, C.S. Cha, Powder microelectrodes I. Reversible systems. Acta Phys. Chim. Sin. **4**(2), 167–171 (1988)
190. C.S. Cha, C.M. Li, H.X. Yang, P.F. Liu, Powder microelectrodes. J. Electroanal. Chem. **368**(1–2), 47–54 (1994)
191. C.M. Li, C.S. Cha, Porous carbon composite/enzyme glucose microsensor. Front. Biosci. **9**, 3324–3330 (2004)
192. D.D.D. Ma, C.S. Lee, F.C.K. Au, S.Y. Tong, S.T. Lee, Small-diameter silicon nanowire surfaces. Science **299**(5614), 1874–1877 (2003)
193. C.Q. Sun, H. Xie, W. Zhang, H. Ye, P. Hing, Preferential oxidation of diamond {111}. J. Phys. D-Appl. Phys. **33**(17), 2196–2199 (2000)
194. M.L. Alymov, E.I. Maltina, Y.N. Stepanov, Nanostruct. Mater. **4** (1994)
195. S. Ma, H. Liang, X. Wang, J. Zhou, L. Li, C.Q. Sun, Controlling the band gap of ZnO by programmable annealing. J. Phys. Chem. C **115**(42), 20487–20490 (2011)
196. Y. Hu, O.K. Tan, W.Q. Cao, W.G. Zhu, Fabrication and characterization of nano-sized $SrTiO_3$-based oxygen sensor for near room-temperature operation. IEEE Sens. J. **5**(5), 825–832 (2005)
197. Y. Hu, O.K. Tan, J.S. Pan, X. Yao, A new form of nanosized $SrTiO_3$ material for near-human-body temperature oxygen sensing applications. J. Phys. Chem. B **108**(30), 11214–11218 (2004)

198. M.K. Zayed, H.E. Elsayed-Ali, Condensation on (002) graphite of liquid bismuth far below its bulk melting point. Phys. Rev. B **72**(20), 205426 (2005)
199. Q. Jiang, F.G. Shi, Size-dependent initial sintering temperature of ultrafine particles. J. Mater. Sci. Technol. **14**(2), 171–172 (1998)
200. H. Roder, E. Hahn, H. Brune, J.P. Bucher, K. Kern, Building one-dimensional and 2-dimensional nanostructures by diffusion-controlled aggregation at surfaces. Nature **366**(6451), 141–143 (1993)